

DUAL VIRTUAL ELEMENT METHOD FOR DISCRETE FRACTURES NETWORKS*

ALESSIO FUMAGALLI[†] AND EIRIK KEILEGAVLEN[†]

Abstract. Discrete fracture networks is a key ingredient in the simulation of physical processes which involve fluid flow in the underground, when the surrounding rock matrix is considered impermeous. In this paper we present two different models to compute the pressure field and Darcy velocity in the system. The first allows a normal flow out of a fracture at the intersections, while the second grants also a tangential flow along the intersections. For the numerical discretization, we use the mixed virtual element method as it is known to handle grid elements of, almost, any arbitrary shape. The flexibility of the discretization allows us to loosen the requirements on grid construction, and thus significantly simplify the flow discretization compared to traditional discrete fracture network models. A coarsening algorithm, from the algebraic multigrid literature, is also considered to further speed up the computation. The performance of the method is validated by numerical experiments.

Key words. Porous media, Discrete fracture network, Interface model, Virtual element method.

AMS subject classifications. 76S05, 65N08, 65N30

1. Introduction. In many hard rocks fractures, naturally occurring or engineered, are of a paramount importance to understand and simulate flow paths. The construction of efficient simulation models for flow in fracture networks is therefore of relevance for applications such as energy recovery and storage, waste disposal (nuclear and CO₂), just to name a few [4, 29, 25].

Flow in the fracture planes is usually modeled by Darcy's law [32, 29], or Forchheimer's law if the Reynold number is sufficiently high [21, 30], and it may also be of crucial interest to include flow along intersections in the models [40, 20, 22]. Because of hydraulic aperture, which is several order of magnitude smaller than other characteristic sizes of the problem, from a modeling perspective a fracture may be represented as a two-dimensional plane (generally manifold) [1, 32, 2], embedded in a three-dimensional domain. The set of, possibly intersecting, fractures forms the network where the flow may take place and, usually, is referred as a discrete fracture network (DFN). Depending on how the fractures were created, they may intersect in an arbitrary manner, leading to highly complex simulation geometries. The flow properties of a fracture are determined by its geo-mechanical and geo-chemical history [18], and there can be significant heterogeneities as well as permeability anisotropy in the fracture plane. Infilling processes or geological movements may alter also the composition and orientation of the material presents in the intersections, leaving the latter as a privileged patterns or obstacles for the flow.

One of the main challenge in DFN simulations in complex fracture geometries is the construction of the computational mesh, combined with the subsequent discretization of the flow equations. Depending on the properties of the chosen numerical method, this may put significant constraints on the mesh algorithm, in particular in meshing of fracture intersections [33, 26, 27]. Compared to two-dimensional gridding problems, which by themselves can be non-trivial, gridding of DFN problems is complicated by the requirement, commonly made, that the grids in different fracture

*Submitted to the editors DATE.

Funding: This work was partially funded by the ANIGMA project from the Research Council of Norway (project no. 244129/E20) through the ENERIX program.

[†]Department of Mathematics, University of Bergen, Bergen, Norway (alessio.fumagalli@uib.no, eirik.keilegavlen@uib.no).

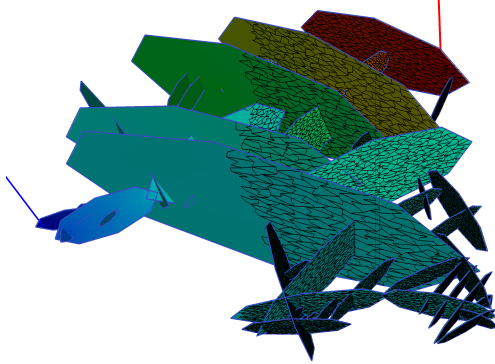


FIG. 1. Example of pressure field in a realistic DFN with several intersecting fractures, represented as ellipses. The fractures are represented by one co-dimensional objects. The blue line represents an injection well, while the red line a production well. Note that the represented mesh is conforming at the intersections. A detailed representation of the grid is reported in [Figure 2](#).

planes are mutually conforming. That is, hanging nodes are not allowed in fracture intersections. The gridding can be simplified by allowing for a relaxed interpretation of the fracture planes [28], in effect locally assigning a curvature to the fracture plane.

If this requirement is loosened, and some of the burden is transferred to an appropriately chosen numerical method, the gridding problem becomes significantly simpler and standard algorithms may be applied to create the global mesh. For instance, the extended finite element method handles discontinuities internal to elements by enriching the approximation space [24, 16, 22]. This removes all requirements on the mesh conforming to fracture intersections, and thus significantly simplifies the gridding [22, 11, 19, 35].

A reasonable compromise between burdening mesh generation and discretization is to require that meshes conform to fracture intersections, but also allow for hanging nodes. This approach allows for the independent construction of a set of bi-dimensional meshes in the fracture planes, which is considerably less difficult than gridding the whole DFN model fully coupled. See [Figure 1](#) and [Figure 2](#) as an example. To further increase the applicability of discretization scheme, it should then allow for general polygonal cells, including hanging nodes. In particular, we note that the virtual element method (VEM) has successfully been applied in the DFN setting [10, 9]. See [8, 6, 14, 5, 3, 7] for a presentation of VEM in various contexts.

In this work, we consider different models to describe the single-phase flow in the network of fractures, with and without the tangential contribution of the intersections included. A reduced model is thus provided, with suitable normal and tangential effective permeabilities, to describe the flow in a two-codimensional framework. We consider a dual formulation of the generalized Darcy problem where the virtual element method is extended to handle the proposed modes. Local mass conservation is thus guaranteed and the normal flux, from each edge in the mesh, may be directly used to simulate the heat or tracer transport in the DFN. A gridding strategy is also presented to generate a conforming mesh, in the sense that the edges may be split to ensure conformity along the intersections of the fractures. The proposed scheme is thus a flexible and robust tool to perform simulations in this context. We present several numerical tests to validate the approach, focusing the study on the order of convergence for the pressure and the velocity in different scenarios.

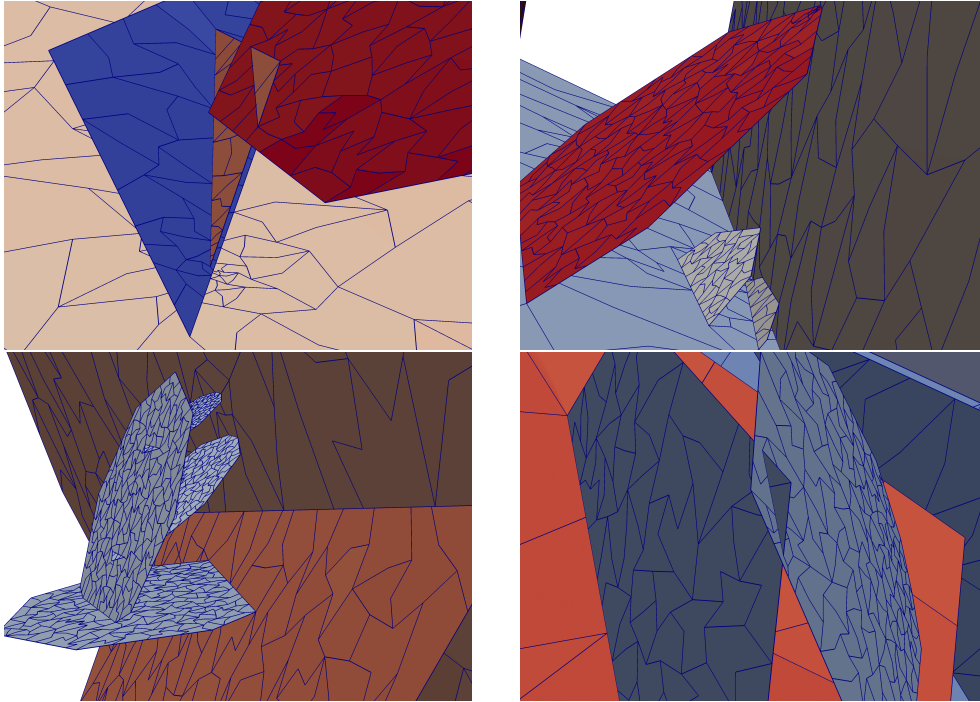


FIG. 2. Four different details of the grid for the example represented in *Figure 1*. The method considered is able to handle these intersection among fractures as conforming.

The paper is organized as follows. The mathematical models and their analyses to describe the fluid flow in the DFN are presented in [section 2](#). [The section 3](#) is devoted to prove the well posedness of the continuous models considered. In [section 4](#) we review the implementation of the mixed virtual element method, and its implementation in a DFN setting. The gridding and coarsening strategy are presented in [section 5](#). Experimental results presented in [section 6](#) mainly consider the error decay of the numerical method presented. Conclusions follow in [section 7](#). [Appendix A](#) briefly describes the coarsening strategy while [Appendix B](#) contains tables related to the examples.

2. Continuous model. This section is devoted to the presentation of the physical model. In [subsection 2.1](#) the setting for single-phase flow is introduced. [subsection 2.2](#) presents the model for a single fracture, while the different couplings among fractures are described in [subsection 2.3](#).

2.1. Single-phase flow in DFN. We make use of the symbol $\sharp(A) \in \mathbb{N}$ indicating the counting measure of A . We define \mathcal{N} the set of indexes associated to the network of fractures, one value identify a fracture. Let us consider $\sharp(\mathcal{N})$ distinct and planar domains Ω_i , for $i \in \mathcal{N}$, embedded in \mathbb{R}^3 such that their union is indicated by $\Omega := \cup_{i \in \mathcal{N}} \Omega_i$. Each polygon represents a fracture and Ω is the discrete fracture network. We indicate by \mathcal{I} the set of indexes associated to the intersection among fractures, one value identify one intersection. We define also the set of one co-dimension intersections among fractures as γ , which can be viewed also as a disjoint union of $\sharp(\mathcal{I})$ lines γ_k such that $\gamma = \cup_{k \in \mathcal{I}} \gamma_k$. We indicate, for each fracture, the finite set of indexes $\mathcal{G}_i := \{k \in \mathbb{N} : \gamma_k \cap \Omega_i \neq \emptyset\}$. We suppose that if $k \in \mathcal{G}_i$ then γ_k belongs to

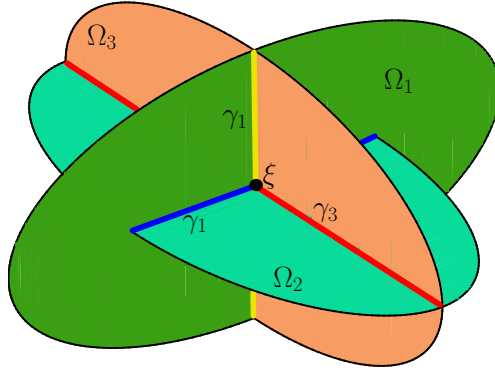


FIG. 3. Example of a DFN with three intersecting fractures, represented as ellipses. The fractures form three one co-dimensional objects, the straight lines, and one two co-dimensional object, the black dot.

the internal part of Ω_i , that is, we assume fractures do not intersect along fracture boundaries. We indicate by \mathcal{P} the set of indexes associated with the intersection of one-codimensional objects, one value identifies one intersection. Finally the set of two co-dimensional intersections among fractures is indicated by ξ , which can be viewed as a union of $\sharp(\mathcal{P})$ points ξ_l such that $\xi = \cup_{l \in \mathcal{P}} \xi_l$. We suppose that if $\xi_l \subset \gamma_k$, for some l and k , then ξ_l belongs to the internal part of γ_k . Note that $\gamma \cup \xi = \cap_{i \in \mathcal{N}} \Omega_i$. The aforementioned sets of indexes are ordered in a natural way. See Figure 3 as an example. Throughout the paper generally, subscripts i and j denote quantities related with fracture planes Ω_i , subscript k is associated with one co-dimensional intersections γ_k , while subscript l is used for two co-dimensional intersections ξ_l . We indicate data and unknowns defined on γ with $\hat{\cdot}$.

Our objective is to compute the pressure field, indicated by p and \hat{p} , and the Darcy velocity field, indicated by \mathbf{u} and $\hat{\mathbf{u}}$, in Ω such that the Darcy equations are fulfilled. To simplify the presentation we start by considering a single fracture Ω_i without intersections. The normal of the fracture is indicated by \mathbf{n}_i , and we define the normal projection matrix as $N_i := \mathbf{n}_i \otimes \mathbf{n}_i$ and the tangential projection matrix as $T_i := I - N_i$. In the following, for each fracture, we make use of tangential divergence and gradient, defined as

$$\nabla_{T_i} \cdot := T_i : \nabla \quad \text{and} \quad \nabla_{T_i} := T_i \nabla.$$

In the sequel, we will sometimes drop the subscript on T_i when there should be no room for confusion.

2.2. Fracture flow. Following the work of [32, 20] we assume that the fracture permeability can be written as a full elliptic second order tensor for the permeability in the tangential space. We adopt a reduced order, or hybrid dimensional, model, to describe p_i and \mathbf{u}_i in the fracture. The model explicitly takes into account the hydraulic aperture d_i of the fracture, which can change in space along the fracture. We require that exist $d_* > 0$ such that $d_i \geq d_*$ for all i , i.e., the fracture does not degenerate. In the forthcoming models we assume that the permeability and fracture aperture are constant in each cell of the computational grid, this is a practical assumption when the discretization is applied. The generalized Darcy equation and

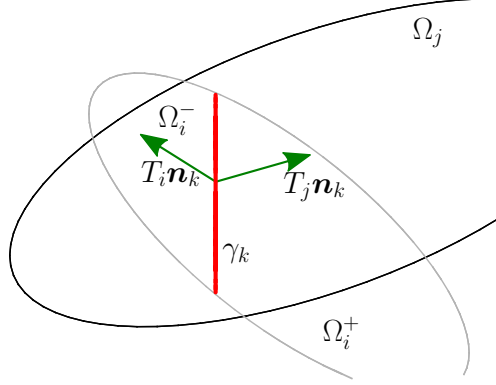


FIG. 4. Example of two fractures with the notation introduced in the derivation of the models.

the conservation of mass in Ω_i can be written as

$$(1) \quad \begin{aligned} \mathbf{u}_i + \lambda_i \nabla p_i &= \mathbf{0} & \text{in } \Omega_i & \quad \text{and} \quad p_i = g_i \text{ on } \partial\Omega_i, \\ \nabla \cdot \mathbf{u}_i &= f_i \end{aligned}$$

where, for each Ω_i , $\lambda_i := d_i k_i$ is the effective permeability, k_i the tangential permeability, f_i the scalar sink or source, and g_i the boundary condition. For simplicity of the proofs, we assume Dirichlet conditions on all fractures, although it would suffice to require only Dirichlet conditions on a non-zero measure portion of the boundary. The case of where some fractures with only Neumann conditions are imposed is studied in the numerical examples. The proofs can also be extended to this case to the price of increased technicalities. Under these assumptions, problem (1) is well posed, see [15].

2.3. Coupling Flow Between Fractures. Now, consider two fractures Ω_i and Ω_j such that a one co-dimensional intersection occurs $\gamma_k = \Omega_i \cap \Omega_j$. We indicate by \mathbf{n}_k the set of unit vectors orthogonal to γ_k . In the internal part of Ω_i , i.e. in $\Omega_i \setminus \gamma_k$, equation (1) is applied and for each internal point of γ_k , far from its possible internal ending, we locally identify two sides of Ω_i indicated Ω_i^+ and Ω_i^- . Since this definition is local, for simplicity we keep uniform notation Ω_i^+ and Ω_i^- for “the same side” of Ω_i . We indicate data and unknowns restricted to one side of a fracture with a + or – superscript. For convenience $\partial\Omega_i$ represents the outer part of the boundary, i.e., without the intersection. We indicate by $T_i \mathbf{n}_k$ the unit normal vector of γ_k lying in the plane of Ω_i and pointing from Ω_i^+ to Ω_i^- . $T_j \mathbf{n}_k$ is defined similarly. See Figure 4 as an example. Following [1, 2], at the intersection we assume the coupling conditions along γ_k as

$$(2) \quad \begin{aligned} \sum_{m=i,j} [\mathbf{u}_m \cdot T_m \mathbf{n}_k]_{\gamma_k} &= 0 & \text{on } \gamma_k, \\ p_i^+|_{\gamma_k} &= p_i^-|_{\gamma_k} = p_j^+|_{\gamma_k} = p_j^-|_{\gamma_k} \end{aligned}$$

where $\cdot|_{\gamma_k}$ is the trace operator from a fracture, Ω_i or Ω_j , to γ_k and $[\cdot]_{\gamma_k}$ denotes the jump operator across γ_k defined as $[\mathbf{u}_m \cdot T_m \mathbf{n}_k]_{\gamma_k} := \mathbf{u}_m^+ \cdot T_m \mathbf{n}_k|_{\gamma_k} - \mathbf{u}_m^- \cdot T_m \mathbf{n}_k|_{\gamma_k}$, for $m = i, j$. Thus, while we allow for flow from Ω_i to Ω_j , the permeability of the intersection is so high, or the width of the fracture so small, that the pressure drop is negligible, see [32] for further considerations.

In subsurface flow, intersections between fractures, or faults, may be significant conduits for fluid flow [36, 34]. It is therefore of interest to extend the model (2) to allow for tangential flow along γ_k and for pressure jumps over the intersection, as studied in *e.g.* [20, 37, 12]. Flow in the intersection is still modeled by a generalized Darcy's law with an additional source term from the surrounding fractures

$$(3a) \quad \begin{aligned} \hat{\mathbf{u}}_k + \hat{\lambda}_k \nabla \hat{p}_k &= \mathbf{0} \\ \nabla \cdot \hat{\mathbf{u}}_k &= \hat{f}_k + \sum_{m=i,j} \llbracket \mathbf{u}_m \cdot T_m \mathbf{n}_k \rrbracket_{\gamma_k} \quad \text{in } \gamma_k \quad \text{and} \quad \begin{aligned} \hat{p}_k &= \hat{g}_k && \text{on } \partial\gamma_k \\ \hat{\mathbf{u}}_k \cdot \mathbf{n}_{\gamma_k} &= 0 && \text{on } \partial\gamma_k^{in} \end{aligned} \end{aligned}$$

where $\hat{\lambda}_k := d_i d_j \hat{k}(\gamma_k)$ is the effective permeability along γ_k , $\hat{k}(\gamma_k)$ is the tangential permeability of γ_k , and \hat{g}_k is the boundary condition on the, possibly empty, outer part (i.e., included in $\partial\Omega_i$ or $\partial\Omega_j$) of the boundary of γ_k , for simplicity, indicated by $\partial\gamma_k$. We define as γ_k^{in} the, possibly empty, part of the boundary of γ_k such that it lies internally to Ω_i or Ω_j . We identify by \mathbf{n}_{γ_k} the unit vector tangential to the intersection pointing outward with respect to $\partial\gamma_k^{in}$. Note that d_i , respectively d_j , is the aperture of fracture Ω_i , respectively Ω_j . Their product represents the measure of the area normal to the intersection. The differential operators are now defined along γ_k and can be written in terms of local coordinates. The coupling condition (2) is generalized, for $m = i, j$, as

$$(3b) \quad \begin{aligned} \mathbf{u}_m^+ \cdot T_m \mathbf{n}_k|_{\gamma_k} &= -\tilde{\lambda}_m (\hat{p}_k - p_m^+|_{\gamma_k}) \\ \mathbf{u}_m^- \cdot T_m \mathbf{n}_k|_{\gamma_k} &= -\tilde{\lambda}_m (p_m^-|_{\gamma_k} - \hat{p}_k) \end{aligned} \quad \text{in } \gamma_k$$

where $\tilde{\lambda}_m := \tilde{k}(\gamma_k)/d_m$ is the effective permeability of the fracture Ω_m in the direction normal to the intersection γ_k , and $\tilde{k}(\gamma_k)$ is the normal permeability of γ_k . Note that it is possible to have different normal permeability for each fracture and even for each side of a fracture, however to avoid confusion we assume a unique value for $\tilde{k}(\gamma_k)$. Following [16, 20] the coupling conditions (3b) can be written as

$$\begin{aligned} \llbracket p_m \rrbracket_{\gamma_k} &= \tilde{\lambda}_m^{-1} (\mathbf{u}_m^+ \cdot T_m \mathbf{n}_k|_{\gamma_k} + \mathbf{u}_m^- \cdot T_m \mathbf{n}_k|_{\gamma_k}) \\ \llbracket \mathbf{u}_m \cdot T_m \mathbf{n}_k \rrbracket_{\gamma_k} &= \tilde{\lambda}_m (p_m^+ + p_m^-) \end{aligned} \quad \text{in } \gamma_k$$

where the jump of pressure and velocity across γ_k are explicitly written.

Finally, considering a single two co-dimensional intersection between fractures, we have $\xi_l = \gamma_k \cap \gamma_n$. Following the idea proposed in [12] we require the same model presented in (2) at the intersection, we have

$$(4) \quad \begin{aligned} \sum_{m=k,n} \llbracket \hat{\mathbf{u}}_m \cdot T_m \mathbf{n}_l \rrbracket_{\xi_l} &= 0 \\ \hat{p}_k^+|_{\xi_l} = \hat{p}_k^-|_{\xi_l} = \hat{p}_n^+|_{\xi_l} = \hat{p}_n^-|_{\xi_l} \end{aligned} \quad \text{in } \xi_l$$

where $\cdot|_{\xi_l}$ is the trace operator from a one co-dimensional intersection to ξ_l and $T_m \mathbf{n}_l$ is a unit vector, pointing outward from ξ_l , and lying on γ_m . While it is possible to extend the model to allow for jumps in pressure and velocity over ξ_l , see [20, 22], this is not considered herein.

We can now define two problems defined on the network Ω which will be used in the sequel. The first problem considers continuous coupling conditions at the fracture intersections, it is the following.

PROBLEM 1 (DFN Darcy flow - continuous coupling). *Considering the aforementioned data and assumptions on Ω , the model problem with continuous coupling conditions is to find (\mathbf{u}, p) in Ω such that (1) is valid for all $i \in \mathcal{N}$ and (2) is valid for all $k \in \mathcal{I}$.*

The second problem allows a flow tangential to the fracture intersection and a possible pressure jump across the one co-dimensional intersections.

PROBLEM 2 (DFN Darcy flow - discontinuous coupling). *Considering the aforementioned data and assumptions on Ω , the model problem with discontinuous coupling conditions is to find (\mathbf{u}, p) in Ω such that (1) is valid for all $i \in \mathcal{N}$, (3) is valid for all $k \in \mathcal{I}$, and (4) is valid for all $l \in \mathcal{P}$.*

REMARK 1. *In the case that γ_k is the one co-dimensional intersection of more than two fractures, coupling conditions (2) can be generalized extending the summation of the normal fluxes on all the fractures and assuming the pressure continuity at the intersection. A similar consideration can be done for the coupling conditions (3) where the summation is extended to all the fractures involved and the definition of $\hat{\lambda}_k$ should include the measure of the cross section of γ_k , now simply represented as a rectangle.*

REMARK 2. *In the case that ξ_l is the two co-dimensional intersection of more than two fractures, coupling conditions (4) can be generalized assuming the pressure continuity at the intersection for all the one co-dimensional objects.*

3. Well posedness. In this part the weak formulation of the problem **Problem 1** and **Problem 2** and the related functional spaces are introduced. We provide also well posedness results for both problems.

3.1. DFN Darcy flow - continuous coupling. We define $\|\cdot\|_E : L^2(E) \rightarrow \mathbb{R}$ as the usual L^2 -norm and $(\cdot, \cdot)_E : L^2(E) \times L^2(E) \rightarrow \mathbb{R}$ which is the usual L^2 -scalar product. To simplify the presentation we use this notation for both scalar and vector functions. We indicate by $[\cdot]_i$ and $[\cdot]_{ij}$ the i -th, respectively ij -th, component of the vector, respectively of the matrix, in the square brackets. We assume also pressure boundary conditions assigned to each $\partial\Omega_i$ by a function $g_i \in H^{\frac{1}{2}}(\partial\Omega_i)$, a source term $f_i \in L^2(\Omega_i)$, and $[\lambda_i]_{jk} \in L^\infty(\Omega_i)$. Given a regular domain $E \in \Omega_i$, we define the functional spaces $Q(E) := L^2(E)$ for the scalar fields and $V(E) := \{\mathbf{v} \in [L^2(E)]^3 : \nabla \cdot \mathbf{v} \in L^2(E)\}$ for the vector fields, which are Hilbert spaces. It is worth to remember that we are dealing with differential operators on the tangent planes of the fractures. With an abuse of notation we write $V_i = V(\Omega_i)$ and $Q_i = Q(\Omega_i)$ for each fracture. We endow Q_i with the usual L^2 -norm and V_i with the H_{div} -norm on the tangent space, defined as $\|\mathbf{v}\|_{V_i}^2 := \|\mathbf{v}\|_{\Omega_i}^2 + \|\nabla \cdot \mathbf{v}\|_{\Omega_i}^2$. The global spaces for the network Ω are defined as $Q(\Omega) := \prod_{i \in \mathcal{N}} Q_i$ with norm and $V(\Omega) := \prod_{i \in \mathcal{N}} V_i$, with an abuse of notation we indicate $V = V(\Omega)$ and $Q = Q(\Omega)$. Their norms are defined as $\|q\|_Q^2 := \sum_{i \in \mathcal{N}} \|q_i\|_{Q_i}^2$ and $\|\mathbf{v}\|_V^2 := \sum_{i \in \mathcal{N}} \|\mathbf{v}_i\|_{V_i}^2$. Following the standard procedure we can derive the weak formulation of **Problem 1** which requires the definition of the following bilinear forms

$$\begin{aligned}
 a(\cdot, \cdot) : V \times V \rightarrow \mathbb{R} : \quad a(\mathbf{u}, \mathbf{v}) &:= \sum_{i \in \mathcal{N}} a_i(\mathbf{u}_i, \mathbf{v}_i), \quad a_i(\mathbf{u}_i, \mathbf{v}_i) := (\lambda_i^{-1} \mathbf{u}_i, \mathbf{v}_i)_{\Omega_i} \\
 b(\cdot, \cdot) : V \times Q \rightarrow \mathbb{R} : \quad b(\mathbf{u}, q) &:= \sum_{i \in \mathcal{N}} b_i(\mathbf{u}_i, q_i), \quad b_i(\mathbf{u}_i, q_i) := -(\nabla \cdot \mathbf{u}_i, q_i)_{\Omega_i}
 \end{aligned}$$

and the following functionals which include the boundary data of the problem and the scalar source term

$$B(\cdot) : V \rightarrow \mathbb{R} : \quad B(\mathbf{v}) := - \sum_{i \in \mathcal{N}} \langle \mathbf{v}_i \cdot \mathbf{n}_{\partial\Omega_i}, g_i \rangle_{\partial\Omega_i}$$

$$F(\cdot) : Q \rightarrow \mathbb{R} : \quad F(q) := - \sum_{i \in \mathcal{N}} (q_i, f_i)_{\Omega_i}$$

where the dual pairing is defined as $\langle \cdot, \cdot \rangle_{\partial\Omega_i} : H^{-\frac{1}{2}}(\partial\Omega_i) \times H^{\frac{1}{2}}(\partial\Omega_i) \rightarrow \mathbb{R}$ and $\mathbf{n}_{\partial\Omega_i}$ is the unit normal pointing outward from $\partial\Omega_i$ and tangent to Ω_i . With this definitions we introduce the following problem.

PROBLEM 3 (Weak formulation of **Problem 1**). *The weak formulation of **Problem 1** is to find $(\mathbf{u}, p) \in V \times Q$ such that*

$$(5) \quad \begin{aligned} a(\mathbf{u}, \mathbf{v}) + b(\mathbf{v}, p) &= B(\mathbf{v}) & \forall \mathbf{v} \in V \\ b(\mathbf{u}, q) &= F(q) & \forall q \in Q \end{aligned}$$

THEOREM 1. ***Problem 3** is well posed.*

Proof. Using standard arguments, mainly Cauchy-Schwarz inequality, it is possible to prove the boundedness, and then the continuity, of the bilinear forms a and b on their spaces as well as the functionals F and B . To show coercivity of a , on the kernel of b we consider a function $\mathbf{w} \in V$ such that $b(\mathbf{w}, q) = 0$ for all $q \in Q$. We then have $\nabla_{T_i} \cdot \mathbf{w}_i = 0$ almost everywhere in Ω_i and $\|\mathbf{w}\|_V^2 = \sum_{i \in \mathcal{N}} \|\mathbf{w}_i\|_{\Omega_i}^2$, thus

$$a(\mathbf{w}, \mathbf{w}) = \sum_{i \in \mathcal{N}} (\lambda_i^{-1} \mathbf{w}_i, \mathbf{w}_i)_{\Omega_i} \gtrsim \|\mathbf{w}\|_V^2.$$

To simplify the proof we now consider only two fractures, being the case of multiple fractures a straightforward extension where the following techniques are properly applied to each fracture intersection. To verify the inf-sup condition on b we can have two possibilities: either the intersection does not reach the boundary of the fracture or its contrary. In both cases, let q be a function in Q and consider the following auxiliary problem

$$\begin{aligned} -\nabla_{T_i} \cdot \nabla_{T_i} \varphi_i &= q_i & \text{in } \Omega_i \\ \varphi_i &= 0 & \text{on } \partial\Omega_i \cup \{\gamma \cap \Omega_i\} \end{aligned}$$

which are decoupled problems, one for each fracture. If the intersection completely cuts Ω_i then, following [17] the previous problem admits a unique solution on each disconnected part of Ω_i , called Ω_i^* . We have $\varphi_i^* \in H^2(\Omega_i^*) \forall i$, such that $\|\varphi_i^*\|_{H^2(\Omega_i^*)} \lesssim \|q_i\|_{\Omega_i^*}$. With an abuse of notation, indicating the H^2 -broken norm with the same symbol, we obtain $\|\varphi_i\|_{H^2(\Omega_i)} \lesssim \|q_i\|_{\Omega_i}$. We consider now $\mathbf{v} \in V$ such that $\mathbf{v}|_{\Omega_i^*} = \nabla_{T_i} \varphi_i^*$, we have $-\nabla_{T_i} \cdot \mathbf{v}|_{\Omega_i^*} = q_i$ in Ω_i^* and

$$\|\mathbf{v}\|_V^2 = \sum_{i \in \mathcal{N}} \|\nabla_{T_i} \varphi_i\|_{\Omega_i}^2 + \|q_i\|_{\Omega_i}^2 \lesssim \|q\|_Q^2.$$

With this choice of \mathbf{v} we obtain the boundedness from below of the bilinear form b

$$b(\mathbf{v}, q) = \sum_{i \in \mathcal{N}} -(\nabla_{T_i} \cdot \mathbf{v}, q)_{\Omega_i} = \|q\|_Q^2 \gtrsim \|q\|_Q \|\mathbf{v}\|_V.$$

Following [15] we conclude that in the case where the intersection boundaries coincide with the boundary of the fracture planes, [Problem 3](#) is well posed. We consider now the problem of partially immersed intersection, *i.e.*, one ending part touches a fracture boundary and the other is immersed in the fracture. The fully immersed intersection is a straightforward extension, where the same technique is applied to both the ending parts. If the intersection is immersed in the fracture planes, following [17, 23] the previous auxiliary problem admits a unique solution $\varphi_i \in H^{\frac{3}{2}-\epsilon}(\Omega_i)$, $\epsilon > 0$ and for all $i \in \mathcal{N}$. Define a regularized kernel $\theta \in C^\infty(T\Omega_i)$ with compact support in $T\Omega_i$, that is, the tangent space of Ω_i , centred in the immersed part of γ . We introduce also the corresponding family of mollifiers $\theta_\zeta(x) = \zeta^{-n}\theta(x/\zeta)$ for $\zeta > 0$ and $n \in \mathbb{N}$. We consider now $\mathbf{v}_\zeta \in V \cap C^\infty(T\Omega_i)$ such that $[\mathbf{v}_\zeta]_j = \phi_\zeta * [\nabla_{T_i}\varphi_i]_j$ for $j = 1, 2$. We have

$$\|\mathbf{v}_\zeta\|_V^2 = \|\theta_\zeta * \nabla_{T_i}\varphi_i\|_{\Omega_i}^2 + \|\nabla_{T_i} \cdot \theta_\zeta * \nabla_{T_i}\varphi_i\|_{\Omega_i}^2$$

where, with an abuse of notation, the mollifier is applied to each component of \mathbf{v}_i . Using the properties of the mollifiers, we can bound the first term as

$$\|\theta_\zeta * \nabla_{T_i}\varphi_i\|_{\Omega_i} \leq \|\nabla_{T_i}\varphi_i\|_{\Omega_i} \leq \|\varphi_i\|_{H^1(\Omega_i)} \leq \|q\|_{\Omega_i},$$

while the second term can be estimated as

$$\|\nabla_{T_i} \cdot \theta_\zeta * \nabla_{T_i}\varphi_i\|_{\Omega_i} = \|\theta_\zeta * \nabla_{T_i} \cdot \nabla_{T_i}\varphi_i\|_{\Omega_i} \leq \|\nabla_{T_i} \cdot \nabla_{T_i}\varphi_i\|_{\Omega_i} = \|q\|_{\Omega_i}.$$

We obtain $\|\mathbf{v}_\zeta\|_V \lesssim \|q_i\|_Q$. With this choice we have for a Ω_i

$$\begin{aligned} b_i(\mathbf{v}_\zeta, q_i) &= -(\nabla_{T_i} \cdot \mathbf{v}_\zeta, q_i)_{\Omega_i} = -(\nabla_{T_i} \cdot \theta_\zeta * \nabla_{T_i}\varphi_i, q_i)_{\Omega_i} = \\ &= -(\theta_\zeta * \nabla_{T_i} \cdot \nabla_{T_i}\varphi_i, q_i)_{\Omega_i} = (\theta_\zeta * q_i, q_i)_{\Omega_i}. \end{aligned}$$

Using again the property of the mollifiers we obtain that for $n \rightarrow \infty$: $\mathbf{v}_\zeta \xrightarrow{L^2} \mathbf{v}$, with $\mathbf{v} \in V$, and $\theta_\zeta * q_i \xrightarrow{L^2} q_i$. Following [15] we conclude also in this case that [Problem 3](#) is well posed. \square

3.2. DFN Darcy flow - discontinuous coupling. We consider now the functional setting to present the weak formulation of problem [Problem 2](#). Referring to [\(3a\)](#) and [\(3b\)](#), we assume pressure boundary conditions assigned to each ending point $\partial\gamma_k$ by a scalar $\hat{g}_i \in \mathbb{R}$, a source term defined in $\hat{f}_k \in L^2(\gamma_k)$, an effective tangential permeability in $\hat{\lambda}_k \in L^\infty(\gamma_k)$, and an effective normal permeability with regularity $\tilde{\lambda}_m \in L^\infty(\gamma_k)$. Motivated by *e.g.* [32], we introduce a new family of spaces, one for each fracture Ω_i by

$$W_i := \{\mathbf{v} \in V_i : \mathbf{v}^+ \cdot T_i \mathbf{n}_k|_{\gamma_k} \in L^2(\gamma_k) \text{ and } \mathbf{v}^- \cdot T_i \mathbf{n}_k|_{\gamma_k} \in L^2(\gamma_k), \forall k \in \mathcal{G}_i\}$$

and their composition for the vector fields $W := \prod_{i \in \mathcal{N}} W_i$, which are Hilbert spaces endowed with norms

$$\|\mathbf{v}\|_{W_i}^2 := \|\mathbf{v}\|_{V_i}^2 + \sum_{k \in \mathcal{G}_i} \|\mathbf{v}^+ \cdot T_i \mathbf{n}_k\|_{\gamma_k}^2 + \|\mathbf{v}^- \cdot T_i \mathbf{n}_k\|_{\gamma_k}^2 \quad \text{and} \quad \|\mathbf{v}\|_W^2 := \sum_{i \in \mathcal{N}} \|\mathbf{v}_i\|_{W_i}^2.$$

It is worth to notice that we require more regularity on the intersections for W_i than V_i , where implicitly we assume $H^{-1/2}$ -regularity, in order to properly take into account the coupling conditions [\(3b\)](#). This assumption is related to Robin-type boundary

conditions for problem in mixed form, see [32] for a more detailed investigation. For the intersections we introduce the functional spaces for both scalar fields as $\hat{Q}_k := L^2(\gamma_k)$, with the usual L^2 -norm, and vector fields as

$$\hat{V}_k := \{\hat{\mathbf{v}} \in [L^2(\gamma_k)]^3 : \nabla \cdot \hat{\mathbf{v}} \in L^2(\gamma_k)\} \quad \text{with} \quad \|\hat{\mathbf{v}}\|_{\hat{V}_k}^2 := \|\hat{\mathbf{v}}\|_{\gamma_k}^2 + \|\nabla \cdot \hat{\mathbf{v}}\|_{\gamma_k}^2.$$

The global spaces are $\hat{V} := \prod_{k \in \mathcal{I}} \hat{V}_k$, with norm $\|\hat{\mathbf{v}}\|_{\hat{V}}^2 := \sum_{k \in \mathcal{I}} \|\hat{\mathbf{v}}_k\|_{\hat{V}_k}^2$ for the vector fields, and $\hat{Q} := \prod_{k \in \mathcal{I}} \hat{Q}_k$, with norm $\|\hat{q}\|_{\hat{Q}}^2 := \sum_{k \in \mathcal{I}} \|\hat{q}_k\|_{\hat{Q}_k}^2$ for the scalar fields. Finally the spaces for the coupled problem are $U := W \times \hat{V}$, with induced norm from W and \hat{V} , and $O := Q \times \hat{Q}$, with induced norm from Q and \hat{Q} . All the aforementioned spaces are Hilbert spaces. We introduce the bilinear forms associated with the intersections as

$$\begin{aligned} \hat{a}(\cdot, \cdot) : \hat{V} \times \hat{V} &\rightarrow \mathbb{R} : \quad \hat{a}(\hat{\mathbf{u}}, \hat{\mathbf{v}}) := \sum_{k \in \mathcal{I}} \hat{a}_k(\hat{\mathbf{u}}_k, \hat{\mathbf{v}}_k), \quad \hat{a}_k(\hat{\mathbf{u}}_k, \hat{\mathbf{v}}_k) := \left(\hat{\lambda}_k^{-1} \hat{\mathbf{u}}_k, \hat{\mathbf{v}}_k \right)_{\gamma_k} \\ \hat{b}(\cdot, \cdot) : \hat{V} \times \hat{Q} &\rightarrow \mathbb{R} : \quad \hat{b}(\hat{\mathbf{u}}, \hat{q}) := \sum_{k \in \mathcal{I}} \hat{b}_k(\hat{\mathbf{u}}_k, \hat{q}_k), \quad \hat{b}_k(\hat{\mathbf{u}}_k, \hat{q}_k) := -(\nabla \cdot \hat{\mathbf{u}}_k, \hat{q}_k)_{\gamma_k}. \end{aligned}$$

The global bilinear forms for the coupled problem are $\alpha(\cdot, \cdot) : U \times U \rightarrow \mathbb{R}$ and $\beta(\cdot, \cdot) : U \times O \rightarrow \mathbb{R}$

$$\begin{aligned} \alpha((\mathbf{u}, \hat{\mathbf{u}}), (\mathbf{v}, \hat{\mathbf{v}})) &:= a(\mathbf{u}, \mathbf{v}) + \hat{a}(\hat{\mathbf{u}}, \hat{\mathbf{v}}) + cc_1^+(\mathbf{u}, \mathbf{v}) + cc_1^-(\mathbf{u}, \mathbf{v}) \\ \beta((\mathbf{u}, \hat{\mathbf{u}}), (q, \hat{q})) &:= b(\mathbf{u}, q) + \hat{b}(\hat{\mathbf{u}}, \hat{q}) + cc_2(\mathbf{u}, \hat{q}) \end{aligned}$$

where the bilinear forms associated with the coupling conditions are

$$(6) \quad cc_1^+(\cdot, \cdot) : V \times V \rightarrow \mathbb{R} : \quad cc_1^+(\mathbf{u}, \mathbf{v}) := \sum_{i \in \mathcal{N}} \sum_{j \in \mathcal{G}_i} \left(\tilde{\lambda}_i^{-1} \mathbf{u}_i^+ \cdot T_i \mathbf{n}_j, \mathbf{v}_i^+ \cdot T_i \mathbf{n}_j \right)_{\gamma_j}$$

$$(7) \quad cc_2(\cdot, \cdot) : V \times \hat{Q} \rightarrow \mathbb{R} : \quad cc_2(\mathbf{u}, \hat{q}) := \sum_{i \in \mathcal{N}} \sum_{j \in \mathcal{G}_i} \left(\llbracket \mathbf{u}_i \cdot T_i \mathbf{n}_j \rrbracket_{\gamma_j}, \hat{q}_j \right)_{\gamma_j},$$

$cc_1^-(\cdot, \cdot)$ follow immediatly. The functional B is extended naturally on U and we define

$$\Phi : O \rightarrow \mathbb{R} : \quad \Phi((q, \hat{q})) := - \sum_{i \in \mathcal{N}} (q_i, f_i)_{\Omega_i} - \sum_{k \in \mathcal{I}} \left(\hat{q}_k, \hat{f}_k \right)_{\gamma_k}$$

PROBLEM 4 (Weak formulation of [Problem 2](#)). *The weak formulation of [Problem 2](#) is to find $((\mathbf{u}, \hat{\mathbf{u}}), (p, \hat{p})) \in U \times O$ such that*

$$(8) \quad \begin{aligned} \alpha((\mathbf{u}, \hat{\mathbf{u}}), (\mathbf{v}, \hat{\mathbf{v}})) + \beta((\mathbf{v}, \hat{\mathbf{v}}), (p, \hat{p})) &= B((\mathbf{v}, \hat{\mathbf{v}})) \quad \forall (\mathbf{v}, \hat{\mathbf{v}}) \in U \\ \beta((\mathbf{u}, \hat{\mathbf{u}}), (q, \hat{q})) &= \Phi((q, \hat{q})) \quad \forall (q, \hat{q}) \in O \end{aligned}$$

THEOREM 2. *[Problem 4](#) is well posed.*

Proof. Using standard arguments, mainly Cauchy-Schwarz inequality, it is possible to prove the boundedness, and then the continuity, of the bilinear forms α and β on their spaces as well as the functionals Φ and B . Considering a function $(\mathbf{w}, \hat{\mathbf{w}}) \in U$ such that $\beta((\mathbf{w}, \hat{\mathbf{w}}), (q, \hat{q})) = 0$ for all $(q, \hat{q}) \in O$, we have $\nabla_{T_i} \cdot \mathbf{w}_i = 0$ almost everywhere in Ω_i and $\nabla \cdot \hat{\mathbf{w}}_k = 0$ almost everywhere in γ_k . The norm of $(\mathbf{w}, \hat{\mathbf{w}})$ becomes

$$\|(\mathbf{w}, \hat{\mathbf{w}})\|_U^2 = \sum_{i \in \mathcal{N}} \|\mathbf{w}_i\|_{\Omega_i}^2 + \sum_{k \in \mathcal{G}_i} \|\mathbf{w}_i^+ \cdot T_i \mathbf{n}_k\|_{\gamma_k}^2 + \|\mathbf{w}_i^- \cdot T_i \mathbf{n}_k\|_{\gamma_k}^2 + \sum_{k \in \mathcal{I}} \|\hat{\mathbf{w}}_k\|_{\gamma_k}^2.$$

It is possible to show that $\alpha((\mathbf{w}, \hat{\mathbf{w}}), (\mathbf{w}, \hat{\mathbf{w}})) \gtrsim \|(\mathbf{w}, \hat{\mathbf{w}})\|_U^2$, thus α is coercive on the kernel of β .

Given a function $(q, \hat{q}) \in O$, taking inspiration from [32, 20], we introduce the following auxiliary problems for fractures

$$\begin{aligned} -\nabla_{T_i} \cdot \nabla_{T_i} \varphi_i &= q_i && \text{in } \Omega_i \\ \nabla_{T_i} \varphi_i^+ \cdot T_i \mathbf{n}_j &= \hat{q}_j && \text{on } \gamma_j, j \in \mathcal{G}_i \\ \nabla_{T_i} \varphi_i^- \cdot T_i \mathbf{n}_j &= -\hat{q}_j && \text{on } \gamma_j, j \in \mathcal{G}_i \\ \llbracket \varphi_i \rrbracket_{\gamma_j} &= 0 && \text{on } \gamma_j, j \in \mathcal{G}_i \\ \varphi_i &= 0 && \text{on } \partial\Omega_i \end{aligned}$$

and for the intersections

$$\begin{aligned} -\nabla \cdot \nabla \hat{\varphi}_k &= \hat{q}_k && \text{in } \gamma_k \\ \hat{\varphi}_k &= 0 && \text{on } \partial\gamma_k \end{aligned}$$

We consider only the case where the intersection reaches the fracture boundary; intersection endpoints inside the fracture plane can be handled similar to the proof of Theorem 1. Following [17] the previous problems admits a unique solution on each disconnected part of Ω_i , indicated by Ω_i^* . In the first case we have $\varphi_i^* \in H^2(\Omega_i^*) \forall i$, such that $\|\varphi_i^*\|_{H^2(\Omega_i^*)} \lesssim \|q_i\|_{\Omega_i^*} + \sum_{j \in \mathcal{G}_i} \|\hat{q}_j\|_{\gamma_j}$. We consider now $\mathbf{v} \in W$ such that $\mathbf{v}|_{\Omega_i^*} = \nabla_{T_i} \varphi_i^*$, we have $-\nabla_{T_i} \cdot \mathbf{v}|_{\Omega_i^*} = q_i$ in Ω_i^* , $\mathbf{v}|_{\Omega_i^*} \cdot T_i \mathbf{n}_j = \hat{q}_j$ for all $j \in \mathcal{G}_i$, and

$$\|\mathbf{v}_i\|_{W_i}^2 = \|\nabla_{T_i} \varphi_i\|_{\Omega_i}^2 + \|q_i\|_{\Omega_i}^2 + 2 \sum_{j \in \mathcal{G}_i} \|\hat{q}_j\|_{\gamma_j}^2 \lesssim \|q_i\|_{Q_i}^2 + \sum_{j \in \mathcal{G}_i} \|\hat{q}_j\|_{Q_j}^2 \leq \|q\|_Q^2 + \|\hat{q}\|_Q^2.$$

For the second family of problems we obtain the existence of $\hat{\varphi}_k \in H^2(\gamma_k) \forall k$, such that $\|\hat{\varphi}_k\|_{H^2(\gamma_k)} \lesssim \|\hat{q}_k\|_{\gamma_k}$. Considering $\hat{\mathbf{v}} \in \hat{V}$ such that $\hat{\mathbf{v}}_k = \nabla \hat{\varphi}_k$, we have $-\nabla \cdot \hat{\mathbf{v}}_k = \hat{q}_k$ and

$$\|\hat{\mathbf{v}}\|_{\hat{V}}^2 = \sum_{k \in \mathcal{I}} \|\nabla_{T_i} \hat{\varphi}_k\|_{\gamma_k}^2 + \|\hat{q}_k\|_{\gamma_k}^2 \lesssim \|\hat{q}\|_Q^2.$$

With this choice of \mathbf{v} and $\hat{\mathbf{v}}$ we obtain the boundedness from below of the bilinear form β

$$\beta((\mathbf{v}, \hat{\mathbf{v}}), (q, \hat{q})) = \sum_{i \in \mathcal{N}} \|q_i\|_{Q_i}^2 + 2 \sum_{j \in \mathcal{G}_i} \|\hat{q}_j\|_{\gamma_j}^2 + \sum_{k \in \mathcal{I}} \|\hat{q}_k\|_{\gamma_k}^2 \gtrsim \|(q, \hat{q})\|_O \|(\mathbf{v}, \hat{\mathbf{v}})\|_U.$$

Thus the inf-sup condition is fulfilled, and following [15] we conclude that **Problem 4** is well posed. \square

4. Discrete approximation. In this part we present the numerical discretization of **Problem 3** and **Problem 4**. We extend the virtual element method for mixed problem presented in [14, 5, 7] to the DFN setting. For simplicity we start the discretization of **Problem 3** considering only the network composed by a single fracture $\Omega = \Omega_i$, the extension of more than one fracture is trivial but requires a heavier notation, while the approximation of (2) will be discussed below. For realistic fracture networks, the solutions will commonly have low regularity due to heterogeneities, and we therefore limit ourselves to lowest order methods.

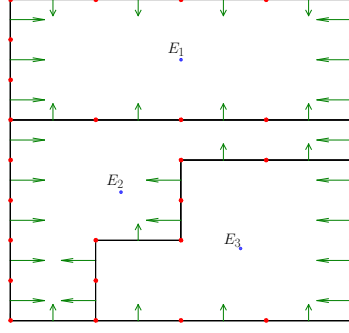


FIG. 5. Example of three elements admitted in the discretization. The blue points represent the centre \mathbf{x}_E for each element E , the red points define the edges e , and the green arrows are the normal vector to the edges. E_1 is a rectangular element but composed of 14 edges and E_2 is a non-convex element.

4.1. Discrete setting. Let us consider $\mathcal{T}(\Omega)$ a tessellation of a single fracture Ω into non-overlapping polygons E and the union of the edges e as $\mathcal{E}(\Omega) = \{e \in \partial E\}$. We denote by h_E the diameter of E , by \mathbf{x}_E the centre of E , by \mathbf{n}_e with $e \in \mathcal{E}(E)$ the unit normal of e pointing outward with respect to the internal part of E , and by h the maximum diameter in $\mathcal{T}(\Omega)$. When there is no room for confusion we write \mathcal{T} instead of $\mathcal{T}(\Omega)$ and \mathcal{E} instead of $\mathcal{E}(\Omega)$. We assume that there exist $\rho_E \in \mathbb{R}^+$ such that E is star-shaped with respect to every point of a disc of radius $\rho_E h_E$ and $|e| \geq \rho_E h_E$, for all $e \in \mathcal{E}(E)$. An example of elements is presented in Figure 5. We introduce the following local spaces for the element E of \mathcal{T} : for the scalar fields $Q_h(E) := \{q \in Q(E) : q \in \mathbb{P}_0(E)\}$ and for the vector fields

$$V_h(E) := \{\mathbf{v} \in V(E) : \mathbf{v} \cdot \mathbf{n}_{e_i}|_{e_i} \in \mathbb{P}_0(e_i) \forall e_i \in \mathcal{E}(E), \nabla \cdot \mathbf{v} \in \mathbb{P}_0(E), \nabla \times \mathbf{v} = \mathbf{0}\}.$$

It is worth to notice that we do not reconstruct the velocity inside an element, since in most of the applications the normal flux from a face is the physical quantity of interest. The global spaces for the fracture Ω are defined by

$$\begin{aligned} Q_h(\Omega) &:= \{q \in Q(\Omega) : q|_E \in Q_h(E) \forall E \in \mathcal{T}\} \\ V_h(\Omega) &:= \{\mathbf{v} \in V(\Omega) : \mathbf{v}|_E \in V_h(E) \forall E \in \mathcal{T}\}. \end{aligned}$$

The degrees of freedom, simply *d.o.f.*'s, for $Q_h(\Omega)$ are constant value in each element of the mesh, while for $\mathbf{v} \in V_h(\Omega)$ we consider

$$(\mathbf{v} \cdot \mathbf{n}_e, q)_e \quad \forall e \in \mathcal{E} \text{ and } \forall q \in \mathbb{P}_0(e).$$

We indicate by $N_{dof} = \#\mathcal{E}(E)$ the number of *d.o.f.*'s for a generic element E . To simplify the presentation, we construct the approximation locally to each element $E \in \mathcal{T}$ and then use the fact that the velocity *d.o.f.*'s are single valued for all $e \in \mathcal{E}$, the global approximation can be build up. When it is clear from the context, we consider the bilinear form introduced in the previous section restricted to an element of the mesh. For the element $E \in \mathcal{T}$ we define the local canonical base for both spaces: for $Q_h(E)$ is trivial, while for $V_h(E)$ we indicate with $\text{base}(V_h(E)) = \{\boldsymbol{\varphi}_\omega\}_{\omega=1}^{N_{dof}}$ such that $\boldsymbol{\varphi}_\omega \in V_h(E)$ and given $\mathbf{v} \in V_h(E)$ we have $\mathbf{v} = \sum_{\omega=1}^{N_{dof}} [\mathbf{v}]_\omega \boldsymbol{\varphi}_\omega$, with $[\mathbf{v}]_\omega \in \mathbb{R}$. As a consequence of these facts we have $(\boldsymbol{\varphi}_\omega \cdot \mathbf{n}_{e_j}, 1)_{e_j} = \delta_{\omega j}$ which means $|e_\omega| \boldsymbol{\varphi}_\omega \cdot \mathbf{n}_{e_\omega} = 1$, as well as $(\nabla \cdot \boldsymbol{\varphi}_\omega, 1)_E = 1$ which means $|E| \nabla \cdot \boldsymbol{\varphi}_\omega = 1$. With these choices, it is

possible to compute directly the bilinear form $b(\cdot, \cdot)$ as well as the functionals $F(\cdot)$ and $B(\cdot)$. However the computation of $a(\cdot, \cdot)$ is more tricky and requires the introduction of a projection operator Π_0 , which gives an approximation of $a(\cdot, \cdot) \approx a_h(\cdot, \cdot)$. We will see that the explicit evaluation of the basis functions φ_i is not needed in the internal part of E , but the request that the order of convergence is preserved when using $a_h(\cdot, \cdot)$ instead of $a(\cdot, \cdot)$. We introduce the following local space

$$\mathcal{V}(E) := \{ \mathbf{v} \in V_h(E) : \mathbf{v} = \lambda \nabla v, \text{ for } v \in \mathbb{P}_1(E) \},$$

where ∇ stands for the tangential gradient on the current fracture. We define the projection operator $\Pi_0 : V(E) \rightarrow \mathcal{V}(E)$ such that $a(\mathbf{v} - \Pi_0 \mathbf{v}, \mathbf{w}) = 0$ for all $\mathbf{w} \in \mathcal{V}(E)$. To introduce the discrete bilinear forms, we start by having for $\mathbf{u}, \mathbf{v} \in V_h(E)$

$$(9) \quad a(\mathbf{u}, \mathbf{v}) = a(\Pi_0 \mathbf{u}, \Pi_0 \mathbf{v}) + a((I - \Pi_0)\mathbf{u}, (I - \Pi_0)\mathbf{v}),$$

since the cross terms are zero due to Π_0 .

4.2. Computation of the local H_{div} -mass matrix. We focus now on the approximation of the first term in (9). Since $\Pi_0 \mathbf{u} \in V_h(E)$, it can be expanded in the canonical base $\Pi_0 \mathbf{u} = \sum_{\omega=1}^{N_{\text{dof}}} [\Pi_0 \mathbf{u}]_{\omega} \varphi_{\omega}$ with $\varphi_{\omega} = \lambda \nabla \varphi_{\omega}$, $\varphi_{\omega} \in \mathbb{P}_1(E)$. The trial function $\Pi_0 \mathbf{v} \in \mathcal{V}$ then $\exists v \in \mathbb{P}_1(E)$ such that $\Pi_0 \mathbf{v} = \lambda \nabla v$. Moreover we can write φ_{ω} , as well as v , using a monomial expansion as

$$\varphi_{\omega} = \sum_{m=1}^2 s_{\omega}^m m_m \quad \text{with} \quad m_m(\mathbf{x}) := \frac{[\mathbf{x}]_m - [\mathbf{x}_E]_m}{h_E} \quad \text{and} \quad s_{\omega}^m \in \mathbb{R}.$$

It is worth to notice that the coordinates in the definition of the monomials are defined in the tangential space of Ω . The reason why $m_0(\mathbf{x}) = 1$ is not included will become clear below. We obtain for ω

$$(\lambda^{-1} \varphi_{\omega}, \mathbf{v})_E = -(\nabla \cdot \varphi_{\omega}, v)_E + \sum_{e \in \mathcal{E}(E)} (\varphi \cdot \mathbf{n}_e, v)_e = -\frac{1}{|E|} (1, v)_E + \frac{1}{|e_{\omega}|} (1, v)_{e_{\omega}},$$

which is computable using the monomial expansion of v . Indeed, by using the monomial expansion for both φ_{ω} and v , we obtain

$$(\lambda^{-1} \varphi_{\omega}, \lambda \nabla m_j)_E = (\nabla \varphi_{\omega}, \lambda \nabla m_j)_E = \sum_{i=1}^2 s_{\omega}^i (\nabla m_i, \lambda \nabla m_j)_E \quad \text{for } j = 1, 2$$

the scalar product in the previous expression is computable. Defining the matrices and vectors $G \in \mathbb{R}^{2 \times 2}$, $\mathbf{f}_{\omega}, \mathbf{s}_{\omega} \in \mathbb{R}^2$, $F \in \mathbb{R}^{2 \times N_{\text{dof}}}$, and $\Pi^* \in \mathbb{R}^{2 \times N_{\text{dof}}}$ as

$$[G]_{ij} := (\lambda \nabla m_i, \nabla m_j)_E, \quad [\mathbf{f}_{\omega}]_i := -\frac{1}{|E|} (1, m_i)_E + \frac{1}{|e_{\omega}|} (1, m_i)_{e_{\omega}},$$

$$\mathbf{s}_{\omega} := [s_{\omega}^1, s_{\omega}^2]^{\top} = G^{-1} \mathbf{f}_{\omega}, \quad F := [\mathbf{f}_1 | \dots | \mathbf{f}_{N_{\text{dof}}}], \quad \Pi^* := G^{-1} F,$$

we have $s_{\omega}^k = [\Pi^*]_{\omega k}$. The final expression thus reads

$$a(\Pi_0 \varphi_{\omega}, \Pi_0 \varphi_{\theta}) = \sum_{i=1}^{N_{\text{dof}}} \sum_{j=1}^{N_{\text{dof}}} s_{\omega}^i s_{\theta}^j (\lambda \nabla m_i, \nabla m_j)_E = \sum_{i=1}^{N_{\text{dof}}} \sum_{j=1}^{N_{\text{dof}}} [\Pi^*]_{\omega i} [G]_{ij} [\Pi^*]_{\theta j} =$$

$$= [(\Pi^*)^{\top} G \Pi^*]_{\omega \theta}.$$

For the second, stability, term in (9), we follow [14, 5, 7] and approximate the term as

$$\begin{aligned} a((I - \Pi_0)\varphi_\omega, (I - \Pi_0)\varphi_\theta) &\approx s((I - \Pi_0)\varphi_\omega, (I - \Pi_0)\varphi_\theta) := \\ &:= \varsigma \sum_{i=1}^{N_{dof}} dof_i((I - \Pi_0)\varphi_\omega) dof_i((I - \Pi_0)\varphi_\theta), \end{aligned}$$

where $s(\cdot, \cdot) : V_h(E) \times V_h(E) \rightarrow \mathbb{R}$ is the bilinear form associated to the stabilization and $\varsigma \in \mathbb{R}$ is a suitable parameter that will be explained later on. We give an expression of $dof_i((I - \Pi_0)\varphi_\omega)$. Since $\mathcal{V} \subset V_h(E)$ we expand each projected element of the canonical base on the canonical base itself, *i.e.* $\Pi_0\varphi_\omega = \sum_{i=1}^{N_{dof}} \pi_\omega^i \varphi_i$ for $\omega = 1, \dots, N_{dof}$ with $\pi_\omega^j = dof_j(\Pi_0\varphi_\omega)$, which is also

$$\Pi_0\varphi_\omega = \sum_{j=1}^2 s_\omega^j \lambda \nabla m_j = \sum_{j=1}^2 s_\omega^j \sum_{i=1}^{N_{dof}} dof_i(\lambda \nabla m_j) \varphi_i = \sum_{i=1}^{N_{dof}} \left(\sum_{j=1}^2 s_\omega^j dof_i(\lambda \nabla m_j) \right) \varphi_i,$$

obtaining π_ω^i equal to the term in the brackets. This is computable introducing the matrix $D \in \mathbb{R}^{2 \times 2}$, with $[D]_{ij} := dof_i(\lambda \nabla m_j)$, as $\pi_\omega^i = [D\Pi^*]_{i\omega}$. For the stabilization we finally obtain $s((I - \Pi_0)\varphi_\omega, (I - \Pi_0)\varphi_\theta) = \varsigma[(I - D\Pi^*)^\top (I - D\Pi^*)]_{\omega\theta}$. Introducing the bilinear form $a_h(\cdot, \cdot) : V_h(E) \times V_h(E) \rightarrow \mathbb{R}$ as

$$\begin{aligned} a_h(\varphi_\omega, \varphi_\theta) &:= a(\Pi_0\varphi_\omega, \Pi_0\varphi_\theta) + s((I - \Pi_0)\varphi_\omega, (I - \Pi_0)\varphi_\theta) = \\ &= [(\Pi^*)^\top G\Pi^* + \varsigma(I - D\Pi^*)^\top (I - D\Pi^*)]_{\omega\theta}, \end{aligned}$$

the local approximation of [Problem 3](#) for a single fracture is

PROBLEM 5 (Local discrete formulation of [Problem 3](#)). *the discrete approximation of the weak problem in E is find $(\mathbf{u}, p) \in V_h(E) \times Q_h(E)$ such that*

$$\begin{aligned} a_h(\mathbf{u}, \varphi_\theta) + b(p, \varphi_\theta) &= -(\varphi_\theta \cdot \mathbf{n}_{\partial\Omega}, g)_{\partial\Omega \cap e_\theta} \quad \forall \varphi_\theta \in \text{base}(V_h(E)) \\ b(1, \mathbf{u}) &= -(f_i, 1)_E \end{aligned}$$

4.3. Fracture intersection. We consider two intersecting fractures Ω_i and Ω_j such that $\gamma_k = \Omega_i \cap \Omega_j$. The general case is extendible with an analogous procedure. We discretize γ_k as the union of consecutive edges of $\mathcal{E}(\Omega_i) \cap \mathcal{E}(\Omega_j)$, indicated by $\mathcal{T}(\gamma_k)$. For each fracture we double the velocity *d.o.f.*'s in $\mathcal{T}(\gamma_k)$. We enforce (2) by using Lagrange multipliers along $\mathcal{T}(\gamma_k)$, one for each edge involved.

If two intersecting fractures are present, then the coupled model [Problem 2](#) can be considered, and we need to introduce a proper discretization also for the intersection as well as for the coupling condition (3b). The procedure for the former is similar to the derivation of the discrete system for the fractures but in a mono-dimensional framework, *i.e.* in $\mathcal{T}(\gamma)$. For simplicity we consider a single two-codimensional object indicated by γ , the extension to multiple intersections is trivial but requires a heavier notation. The approximation of (4) will be discussed below. We consider the discrete spaces $\hat{Q}_h(E) := \left\{ \hat{q} \in \hat{Q}(E) : \hat{q} \in \mathbb{P}_0(E) \right\}$ with $E \in \mathcal{T}(\gamma)$ for the pressure, for the velocity we have

$$\hat{V}_h(E) := \left\{ \hat{\mathbf{v}} \in \hat{V}(E) : \hat{\mathbf{v}} \cdot \mathbf{n}_{e_i}|_{e_i} \in \mathbb{R} \forall e_i \in \mathcal{E}(E), \nabla \cdot \hat{\mathbf{v}} \in \mathbb{P}_0(E), \nabla \times \hat{\mathbf{v}} = \mathbf{0} \right\},$$

where \mathbf{n}_{e_i} is the unit tangential vector of γ which point outward from E . The global spaces $\hat{Q}_h(\gamma)$ and $\hat{V}_h(\gamma)$ follow naturally. The *d.o.f.*'s for $\hat{Q}_h(\Omega)$ are piece-wise constant in each element of $\mathcal{T}(\gamma)$, while for $\hat{\mathbf{v}} \in \hat{V}_h(\gamma)$, given an ending point e of an element E , we consider $\hat{\mathbf{v}} \cdot \mathbf{n}_e|_e$. Also in this case, we introduce a projection operator $\hat{\Pi}_0 : \hat{V}(E) \rightarrow \hat{\mathcal{V}}(E)$ such that $\hat{a}(\hat{\mathbf{v}} - \hat{\Pi}_0 \hat{\mathbf{v}}, \hat{\mathbf{w}}) = 0$ for all $\hat{\mathbf{w}} \in \hat{\mathcal{V}}(E)$ and where

$$\hat{\mathcal{V}}(E) := \left\{ \hat{\mathbf{v}} \in \hat{V}_h(E) : \hat{\mathbf{v}} = \hat{\lambda} \nabla \hat{v}, \text{ for } \hat{v} \in \mathbb{P}_1(E) \right\}.$$

Following the same process described for an element belonging to a fracture mesh, we obtain the local matrix formulation for the H_{div} -mass matrix

$$\hat{a}(\hat{\varphi}_\omega, \hat{\varphi}_\theta) \approx \hat{a}_h(\hat{\varphi}_\omega, \hat{\varphi}_\theta) = \left[(\hat{\Pi}^*)^\top \hat{G} \hat{\Pi}^* + \hat{\zeta} (I - \hat{D} \hat{\Pi}^*)^\top (I - \hat{D} \hat{\Pi}^*) \right]_{\omega\theta}$$

where $\hat{\varphi}_\omega, \hat{\varphi}_\theta$ are elements of the base for $\hat{V}_h(E)$, $\hat{\zeta} \in \mathbb{R}$ is a proper stabilization parameter, and $\hat{\Pi}^*, \hat{G}$, and \hat{D} are suitable matrices. The approximation of the $\hat{b}(\cdot, \cdot)$ bilinear form follows from the definition of the *d.o.f.*'s for the velocity and the pressure. The discrete formulation of the coupling condition presented in (6) can be derived using the *d.o.f.*'s introduced previously. In particular, for each intersection γ_j of a fracture Ω_i , we double the *d.o.f.* associated with the velocity obtaining the discrete form of $\mathbf{u}^+ \cdot T_i \mathbf{n}_j|_{\gamma_j}$ and $\mathbf{u}^- \cdot T_i \mathbf{n}_j|_{\gamma_j}$. With this choice the implementation of (6) is immediate.

In the case where two intersections meet in a point ξ , coupling conditions (4) should be adopted. For each intersection we double the reduced velocity *d.o.f.*'s in ξ and we enforce the condition by using Lagrange multipliers in ξ .

4.4. Stabilization term. To conclude, we discuss now the stabilization parameters ς and $\hat{\zeta}$ introduced previously. Following [14, 5, 7], to obtain a proper error decay we require that exist $\iota_*, \iota^*, \hat{\iota}_*, \hat{\iota}^* \in \mathbb{R}^+$, independent from the discretization size, such that

$$(10) \quad \begin{aligned} \iota_* a(\Pi_0 \mathbf{v}, \Pi_0 \mathbf{v}) &\leq s((I - \Pi_0) \mathbf{v}, (I - \Pi_0) \mathbf{v}) \leq \iota^* a(\Pi_0 \mathbf{v}, \Pi_0 \mathbf{v}) & \forall \mathbf{v} \in V(\Omega) \\ \hat{\iota}_* \hat{a}(\Pi_0 \hat{\mathbf{v}}, \Pi_0 \hat{\mathbf{v}}) &\leq \hat{s}((I - \hat{\Pi}_0) \hat{\mathbf{v}}, (I - \hat{\Pi}_0) \hat{\mathbf{v}}) \leq \hat{\iota}^* \hat{a}(\Pi_0 \hat{\mathbf{v}}, \Pi_0 \hat{\mathbf{v}}) & \forall \hat{\mathbf{v}} \in \hat{V}(\Omega) \end{aligned}$$

The stability term introduced previously for the fractures fulfils automatically the request, however for highly heterogeneous fractures in the permeability a proper scaling is recommended, *e.g.* $\varsigma_i = \|\lambda_i^{-1}\|_{L^\infty(\Omega_i)}$ for each fracture Ω_i . To fulfil the second request in (10) we can compute explicitly the local matrices involved. Given a segment E of length h_E and supposing that the effective permeability $\hat{\lambda}$ is constant in E , we obtain

$$(\hat{\Pi}^*)^\top \hat{G} \hat{\Pi}^* = \frac{h_E}{4\hat{\lambda}} \begin{bmatrix} 1 & -1 \\ -1 & 1 \end{bmatrix} \quad \text{and} \quad (I - \hat{D} \hat{\Pi}^*)^\top (I - \hat{D} \hat{\Pi}^*) = \frac{1}{2} \begin{bmatrix} 1 & 1 \\ 1 & 1 \end{bmatrix}.$$

We see that choosing $\hat{\zeta} = h_E/\hat{\lambda}$ is enough to scale properly the stability term for the intersection.

REMARK 3. *It is important to note that if $\mathbf{u} = \Pi_0 \mathbf{u}$ or $\mathbf{u} = \Pi_0 \mathbf{v}$ we have the identity: $a_h(\mathbf{u}, \mathbf{v}) = a(\mathbf{u}, \mathbf{v})$. The same is valid for the intersection flow.*

5. The computational grid. Realistic fracture networks can have a highly complex geometry, and correspondingly the construction of the computational grid is challenging. In particular, intersections between fractures add complexity, since for

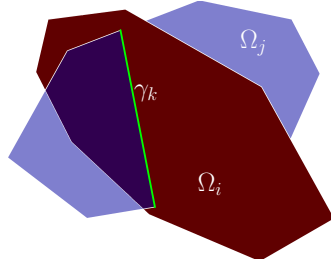


FIG. 6. The geometry of the two fractures and their intersection marked in light green, which are used in this section to present the meshing and coarsening strategy.

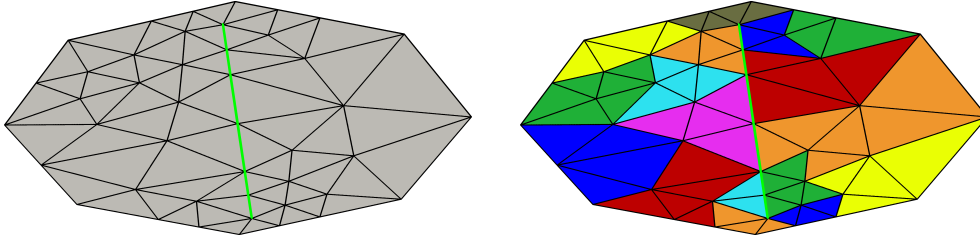


FIG. 7. Left: a triangulated fracture where the intersection is preserved. In general the conformity of the triangles across the intersection is not preserved. Right: Grouping of triangular cells after coarsening. Clusters of triangles with the same colour will form a cell in the coarse mesh.

the types of discretization considered herein, intersections are treated as constraints in the gridding algorithm. This often leads to a high number of cells, and depending on intersection geometry, also low quality elements. The requirement that the grid conforms to intersections can be avoided by using specialized numerical methods, however their implementation tends to be tedious.

Since the virtual element method can handle almost any polygon type, we make two modifications of what can be considered a broadly used DFN meshing algorithm, both aimed at alleviating the computational cost. Other approaches can be found in [33, 26, 28], to name a few. Consider the DFN composed by two intersecting fractures, Ω_i and Ω_j , presented in Figure 6, the extension to several fractures is straightforward. Our first modification is to build each mesh fracture separately and then link them together through the intersection γ_k . This reduces the meshing problem to a set of decoupled 2d domain with internal constraints from the intersection lines, and allows us to apply established 2d meshing software without adaptation for the coupling between domains. We have applied the library Triangle, see [38], which is a fast and robust triangular grid generator that allows for internal constraints. See Figure 7 on the left as an example. The independent meshing also means the fractures can be meshed in parallel.

When a mesh of a fracture is created, our second modification is to coarsen the grid by cell agglomeration so as to lighten the total computational cost. Our approach is motivated by the coarsening in algebraic multigrid methods, *e.g.* [39], and the coarsening is carried out independently for each fracture. As a measure of connectiveness between, we consider a two-point flux approximation (TPFA) discretization of (1), and denote the discretization matrix A . To preserve fracture intersections in the coarse grid, we treat intersections as a boundary for the TPFA discretization, and we explicitly prohibit a coarse cell to cover both sides of the end of an intersection. The

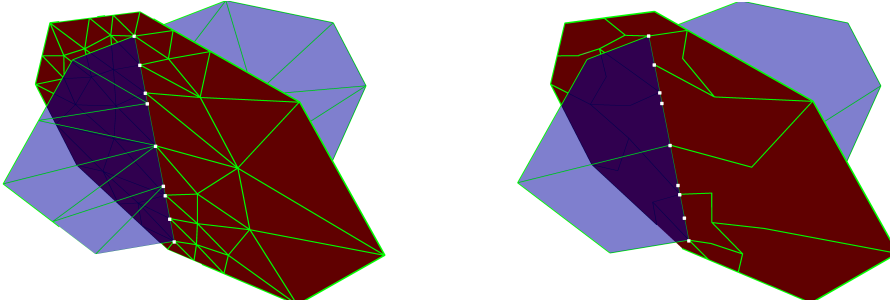


FIG. 8. The meshes of the two fractures linked together before (left) and after (right) coarsening. The points at the intersection are highlighted in white and preserved in the coarsening. The original grid has 93 elements and 153 edges, while the coarse grid has 23 elements and 82 edges. The elements at the intersection are non-matching but conforming.

coarsening ratio is determined by the parameter c_{depth} . Details on the coarsening algorithm can be found in [Appendix A](#), or in the literature on algebraic multigrid methods, see *e.g.* [39].

[Figure 7](#) on the right shows the clustering map after the application of the algorithm. We clearly see that the resulting elements may be concave or even non star-shaped (but a finite union of star-shaped), *e.g.* the big orange element on the right part of the mesh. It is worth to notice that the process of creating and coarsening the meshes is embarrassingly parallel. Once the mesh of each fracture is created, we simply compute a co-refinement of the edges lying on γ_k from both fractures. Splitting the edges of the fractures at the intersection and considering a coherent numeration of the elements and edges the global mesh is build up. Refer to [Figure 8](#) as an example of final mesh with and without the coarsening strategy. The effect of the parameter c_{depth} is illustrated in [Figure 9](#). We also note that in anisotropic media the coarse grid will to some extent adapt to the preferential flow directions, see [Figure 10](#). An example of the grid overlapped to the pressure field is represented in [Figure 1](#) in the introduction.

6. Examples. In this section we validate the models presented in the previous sections through several tests and examples. In particular in [subsection 6.1](#) we highlight the potentiality of the coarsening algorithm presented in [section 5](#) applied in our context. [subsection 6.2](#) contains several tests with a single as well as multiple fractures to put in evidence the error decay and others properties of the numerical solution. In [subsection 6.3](#) we present a numerical example showing the importance to use model presented in [Problem 2](#). Finally in [subsection 6.4](#) we present the solution on a realistic geometry. Our implementation is carried out within the framework of the Matlab Reservoir Simulation Toolbox (MRST) [31].

We make use of the following

$$\text{sparsity} = \frac{\text{nnz}(A)}{\text{size}(A)^2},$$

with $\text{nnz}(A)$ the number of non-zero values of the matrix A and $\text{size}(A)$ the number of rows (or columns) of A , as a measure for the sparsity of a matrix.

6.1. Coarsening. In this subsection we investigate the ability of the coarsening algorithm, introduced in [section 5](#) to generate coarse meshes where the direction of

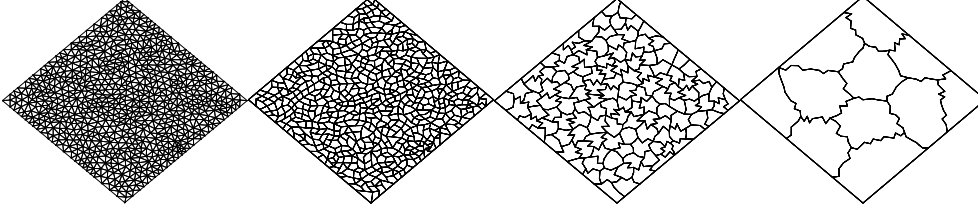


FIG. 9. Example of meshes used for the example in [subsection 6.1](#) with isotropic effective permeability tensor. From the left: triangular mesh, the coarse meshes with $c_{depth} = 1$, $c_{depth} = 3$, and $c_{depth} = 5$, respectively.

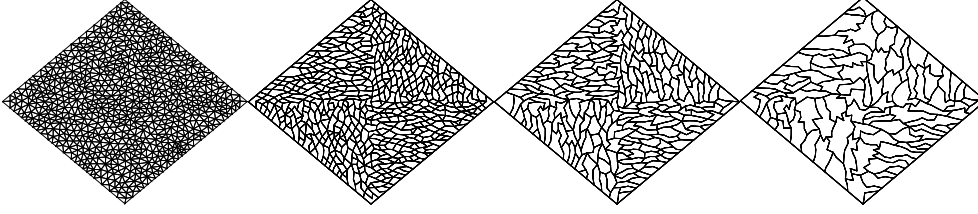


FIG. 10. Example of meshes used for the example in [subsection 6.1](#) for the anisotropic permeability tensor. From the left: triangular mesh, the coarse meshes with $c_{depth} = 1$, $c_{depth} = 3$, and $c_{depth} = 5$, respectively.

the cells reflects the underlying physics. To that end, we consider two problems with different effective permeability: isotropic and anisotropic, the latter in a heterogeneous setting. In both cases we start from a single fracture discretized by a triangular grid, then using the algorithm we coarsen the mesh with different level of refinement: $c_{depth} = 1$, $c_{depth} = 3$, and $c_{depth} = 5$. The fracture is the unit square rotate by $\pi/4$ along the z axis.

In the first case the effective permeability is the identity tensor. [Figure 9](#) shows the meshes obtained with different level of coarsening. The resulting cells of the meshes do not have a preferred alignment. The relative sparsity of the VEM matrix for each coarse level is: $1.4 \cdot 10^{-3}$ for the triangular grid, $3.9 \cdot 10^{-3}$ for $c_{depth} = 1$, $2.3 \cdot 10^{-2}$ for $c_{depth} = 3$, and $2 \cdot 10^{-1}$ for $c_{depth} = 5$, which is a natural effect of this coarsening algorithm. Finally the number of edges (minimum, average, and maximum) and cells for each level is: (3, 5, 6) and 628 for $c_{depth} = 1$, (8, 12, 15) and 122 for $c_{depth} = 3$, and (29, 35, 41) and 11 for $c_{depth} = 5$. The resulting meshes respect the theoretical requests for the VEM.

The second case deals with an anisotropic and heterogeneous effective permeability tensor. We divide the fracture into four sectors: top-left part ($x \leq 0$ and $y > 0$), top-right part ($x > 0$ and $y > 0$), bottom-left part ($x \leq 0$ and $y \leq 0$), and bottom-right part ($x > 0$ and $y \leq 0$). In the first and last sector we set $\lambda = \text{diag}[1, 100]$, while in the others we have $\lambda = \text{diag}[100, 1]$. [Figure 10](#) shows the meshes obtained with different level of coarsening. The resulting cells of the meshes have a preferred alignment related to the underlying permeability which respect both the anisotropy and the heterogeneity. The sparsity of the VEM matrix for each coarse level is: $1.4 \cdot 10^{-3}$ for the triangular grid, $4.5 \cdot 10^{-3}$ for $c_{depth} = 1$, $1.2 \cdot 10^{-2}$ for $c_{depth} = 3$, and $3.1 \cdot 10^{-2}$ for $c_{depth} = 5$, which is a natural effect of this coarsening algorithm. Finally the number of edges (minimum, average, and maximum) and cells for each level is: (3, 5, 8) and 557 for $c_{depth} = 1$, (4, 8, 12) and 236 for $c_{depth} = 3$, and (5, 14, 24) and

95 for $c_{depth} = 5$. Compared with the previous case we notice that the number of cells and the variability in the number of edges is greater, which is needed to preserve the anisotropy of the final mesh. The smaller sparsity of the matrices is a direct consequence of this fact. Also in this case the resulting meshes respect the theoretical requests for the VEM.

We conclude that the coarsening presented in [section 5](#) is a valid tool to create a coarse mesh which is adapted with the underlying physic. In the next examples we consider this coarsening strategy in the computation of error decay.

6.2. Convergence evidence. In this part we present tests that show numerical evidence of convergence of the approximate to the exact solution as well as the order of convergence. In the first part, [subsection 6.2.1](#), a single fracture is considered with different types of meshes. In the second example two intersecting fractures, with coupling conditions described in [Problem 1](#) are applied. Finally two fractures are considered where the flow is described also in their intersection. In the following experiments we make use of the relative errors for both the pressure and the projected velocity, we use the following expressions:

$$err(p) = \frac{\|p - p_{ex}\|_{\Omega}}{\|p_{ex}\|_{\Omega}} \quad \text{and} \quad err(\Pi_0 \mathbf{u}) = \frac{\|\Pi_0 \mathbf{u} - \mathbf{u}_{ex}\|_{\Omega}}{\|\mathbf{u}_{ex}\|_{\Omega}}$$

where p_{ex} and \mathbf{u}_{ex} are the exact solutions computed in the centre of each cell. The same type of errors are computed also for the intersection when the model described in [Problem 2](#) is considered. In addition, furthers details are included in [Appendix B](#).

6.2.1. Single fracture. We consider a single fracture Ω constructed applying a rotation matrix to the points of the unit square $[0, 1]^2$. The rotation is $\pi/4$ along the x axis. We assume unit effective permeability λ and source term equal to

$$f(x, y, z) = 7z - 4 \sin(\pi y) + 2\pi^2 y^2 \sin(\pi y) - 8\pi y \cos(\pi y).$$

We set pressure boundary conditions such that the exact solution of the problem is the following

$$p_{ex}(x, y, z) = x^2 z + 4y^2 \sin(\pi y) - 3z^3.$$

The exact Darcy velocity, in Cartesian coordinates, is

$$\mathbf{u}_{ex}(x, y, z) = \begin{bmatrix} -2xz \\ 0.5(9z^2 - x^2) - 4y \sin(\pi y) - 2\pi y^2 \cos(\pi y) \\ 0.5(9z^2 - x^2) - 4y \sin(\pi y) - 2\pi y^2 \cos(\pi y) \end{bmatrix}.$$

It is possible to verify that $0 \leq p_{ex} \leq 1.337$ in Ω . We consider four different families of grids to analyse the order of convergence for both p and $\Pi_0 \mathbf{u}$, first build in the unit square and then mapped in Ω . We have: Cartesian grids, “coarse grids” where the algorithm from [section 5](#) is applied with $c_{depth} = 2$ on Cartesian grids, triangular grids, and “random grids” where, starting from Cartesian grids, the internal nodes are randomly moved. In the latter a sanity check of the mesh is performed to avoid degenerate cases. See [Figure 11](#) as an example. It is worth to notice that in the case of “coarse grids” and “random grids” the cells may not be convex. In [Figure 12](#) we report the order of convergence for both p and $\Pi_0 \mathbf{u}$ for the four mesh families and we can observe that, in all the cases, the order of convergence respect the decay derived from the theory in [\[7\]](#). [Table 1](#) in [Appendix B](#) reports the detailed values for this example, as well as the sparsity of the matrix, and the minimum and maximum values of the solution. It is interesting to notice that in some cases the discrete maximum or minimum principle is violated.

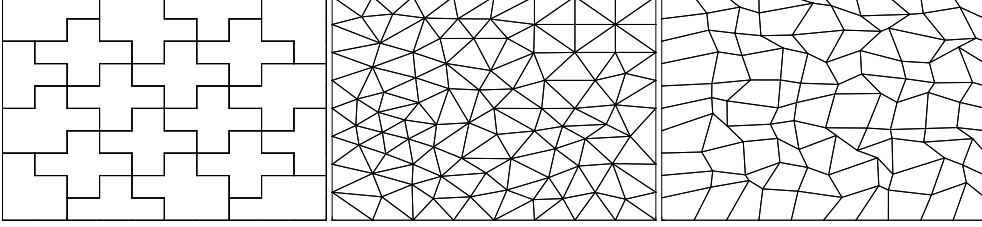


FIG. 11. Example of meshes used for the example in [subsection 6.2.1](#). From the left: coarse mesh, triangular mesh, and random mesh. The pattern of the coarse mesh remains similar for subsequent refinements. The meshes are presented in the (x, y) plane. The Cartesian mesh is omitted.

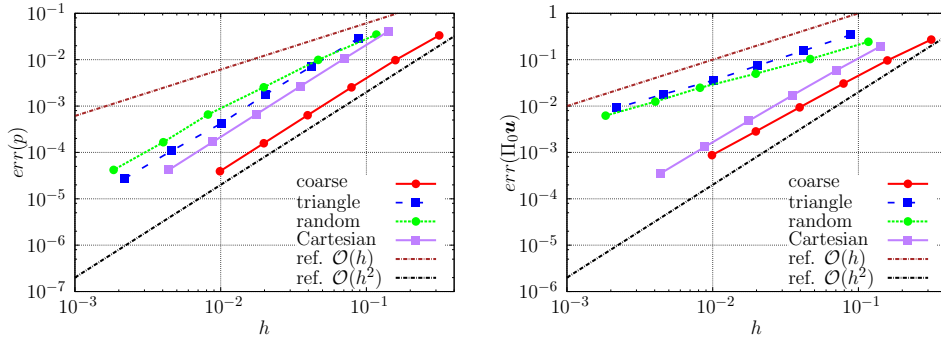


FIG. 12. In the figure the error decay for both p , in the left plot, and $\Pi_0 u$, in the right plot, for the example in [subsection 6.2.1](#). We add the references $\mathcal{O}(h)$ and $\mathcal{O}(h^2)$ to aid the comparison.

6.2.2. Two fractures with intersection. In the second example we analyse the error decay for two intersecting fractures, where [Problem 1](#) is considered. For this test we adapt the problem in Subsubsection 5.3.1 of [\[10\]](#) to our setting. Each fracture is built from an ellipses discretized by 8 segments. We consider two orthogonal fractures, depicted in [Figure 13](#), defined as

$$\begin{aligned}\Omega_1 &= \{(x, y, z) \in \mathbb{R}^3 : z^2 + 4y^2 \leq 1, x = 0\} \\ \Omega_2 &= \{(x, y, z) \in \mathbb{R}^3 : x^2 + 4y^2 \leq 1, z = 0\}.\end{aligned}$$

We assume pressure boundary condition on both $\partial\Omega_1$ and $\partial\Omega_2$, unit effective permeability λ and source as

$$(11) \quad f(x, y, z) = \begin{cases} 8y(1-y) - 8(z-1)^2 & \text{for } z \geq 0 \\ 8y(1-y) - 8(z+1)^2 & \text{for } z < 0 \end{cases} \text{ in } \Omega_1$$

$$f(x, y, z) = \begin{cases} 8y(1-y) - 8(x+\zeta)^2 & \text{for } x \geq 0 \\ 8y(1-y) - 8(x-\zeta)^2 & \text{for } x < 0 \end{cases} \text{ in } \Omega_2$$

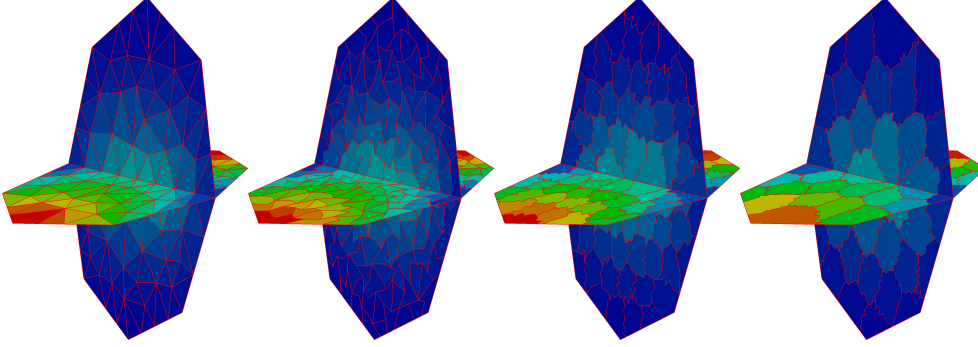


FIG. 13. Example of meshes and numerical solutions for the example in [subsection 6.2.2](#). From the left: triangular mesh, coarse mesh with $c_{depth} = 2$, coarse mesh with $c_{depth} = 4$, and coarse mesh with $c_{depth} = 5$. The solution has range in $[0, 3.6]$ with a “Blue to Red Rainbow” colour map.

With this data the exact solutions p_{ex} and \mathbf{u}_{ex} are

$$(12a) \quad p_{ex}(x, y, z) = \begin{cases} 4y(1-y)(z-1)^2 & \text{for } z \geq 0 \\ 4y(1-y)(z+1)^2 & \text{for } z < 0 \end{cases} \text{ in } \Omega_1$$

$$p_{ex}(x, y, z) = \begin{cases} 4y(1-y)(x+\zeta)^2 & \text{for } x \geq 0 \\ 4y(1-y)(x-\zeta)^2 & \text{for } x < 0 \end{cases} \text{ in } \Omega_2$$

$$(12b) \quad \mathbf{u}_{ex}(x, y, z) = \begin{cases} [0; 8y(z-1)^2; -8y(1-y)(z-1)]^\top & \text{for } z \geq 0 \\ [0; 8y(z+1)^2; -8y(1-y)(z+1)]^\top & \text{for } z < 0 \end{cases} \text{ in } \Omega_1$$

$$\mathbf{u}_{ex}(x, y, z) = \begin{cases} [-8y(1-y)(x+\zeta); 8y(x+\zeta)^2; 0]^\top & \text{for } x \geq 0 \\ [-8y(1-y)(x-\zeta); 8y(x-\zeta)^2; 0]^\top & \text{for } x < 0 \end{cases} \text{ in } \Omega_2,$$

we assume $\zeta = 1$. We consider four different families of discretization to analyse the order of convergence for both p and $\Pi_0 \mathbf{u}$ in both fractures. We have: triangular grids, “coarse grids” with $c_{depth} = 2$, $c_{depth} = 4$, and $c_{depth} = 5$. In all the coarse cases we apply the algorithm from [section 5](#) on triangular grids. See [Figure 13](#) as an example. It is worth to notice that in the case of “coarse grids” the cells may not be convex and even they may be not star-shaped. In [Figure 14](#) we report the L^2 -relative errors for both the projected velocity $\Pi_0 \mathbf{u}$ and the pressure p . We observe that the error decay for the latter is quadratic and the former is linear with respect to the mesh size. Moreover, for the same h , the error is higher for the triangular grid and smaller when c_{depth} increases. One possible explanation is that in the first case each pressure *d.o.f.* is linked with 3 velocity *d.o.f.*'s, while for $c_{depth} = 2$ the average number is 6, for $c_{depth} = 4$ we have 20 edges, and for $c_{depth} = 5$ the average number of edges is 37. This fact can help the accuracy for the meshes with more velocity *d.o.f.*'s. Note that the grid size h reported is the average mesh size, which in some cases exhibits an erratic reduction compared to the steady decrease of the grid size in the triangular grid. [Table 2](#) in [Appendix B](#) reports the detailed values for this example, as well as the sparsity of the matrix, the minimum and maximum values of the solution, number of edges for each cell.

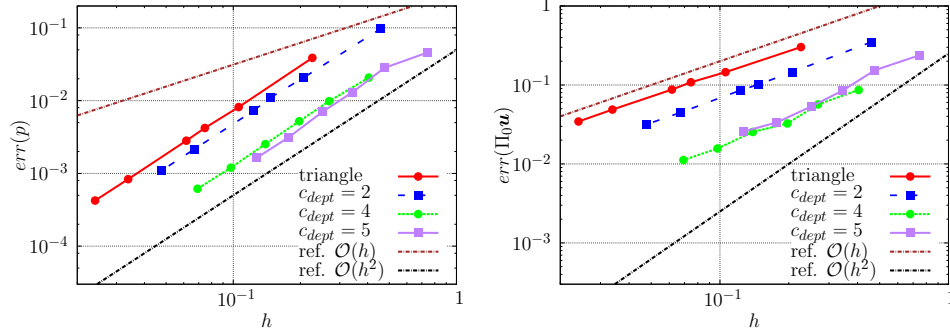


FIG. 14. In the figure the error decay for both p , in the left plot, and $\Pi_0 \mathbf{u}$ for the first example in [subsection 6.2](#). We add the references $\mathcal{O}(h)$ and $\mathcal{O}(h^2)$ to aid the comparison.

REMARK 4. In this test the meshes at the one co-dimensional intersection are matching just because the procedure to construct the two meshes is the same, except the mapping from the reference domain.

6.2.3. Two fractures with intersection flow. In this example we analyse the error decay for the coupled system [Problem 2](#), where two fractures intersect. The fractures Ω_1 and Ω_2 are the same as the test shown in [6.2.2](#), while the intersection γ is defined as $\gamma = \{(x, y, z) \in \mathbb{R}^3 : x = 0, z = 0, y \in [0, 1]\}$. The analytical solution of the problem p_{ex} and \mathbf{u}_{ex} is [\(12\)](#) with $\zeta = -1$ for the fractures and \hat{p}_{ex} and $\hat{\mathbf{u}}_{ex}$ for the intersection

$$\hat{p}_{ex}(x, y, z) = 5y(1 - y) \quad \text{in } \gamma \quad \text{and} \quad \hat{\mathbf{u}}_{ex}(x, y, z) = [0; 5 + 10y; 0]^\top \quad \text{in } \gamma.$$

We consider pressure boundary conditions on both fractures as well as on the intersections. The effective permeability for the fractures and for the intersection is unitary, while the normal effective permeability for the intersection is equal to $\tilde{\lambda} = 8$. The source terms are chosen as [\(11\)](#) with $\zeta = -1$ for the fractures and \hat{q} for the intersection

$$\hat{q}(x, y, z) = 10 + 32y(1 - y) \quad \text{in } \gamma.$$

We consider a family of triangular meshes and two of coarse meshes. The latter are constructed from a triangular mesh with different level of coarsening: $c_{depth} = 2$ and $c_{depth} = 4$. [Figure 15](#) shows a graphical representation of the solution obtained, where also the pressure in the intersection is reported. In [Figure 16](#) we report the L^2 -relative errors for both the projected velocity $\Pi_0 \mathbf{u}$ and the pressure p . We observe that the error decay for the latter is quadratic and the former is linear with respect to the mesh size, for the three families of meshes. In [Figure 17](#) we report the L^2 -relative errors for both the projected velocity $\hat{\Pi}_0 \hat{\mathbf{u}}$ and the pressure \hat{p} for the solution in the intersection γ . The mesh size is now referred to the intersection mesh. Also in this case the slope of the pressure error is nearly quadratic for the three families, but also the velocity (especially for the triangular and coarse- $c_{depth} = 4$ families) has an error that behave quadratically. This is a possible super-convergence property of the numerical scheme in one space dimension. [Table 3](#) and [Table 4](#) in [Appendix B](#) reports the detailed values for this example, as well as the sparsity of the matrix, the minimum and maximum values of the solution, number of edges for each cell.

We conclude the section commenting that in all the tests performed the error decay, for both the pressure and velocity, is coherent with the analyses presented in [\[7\]](#).

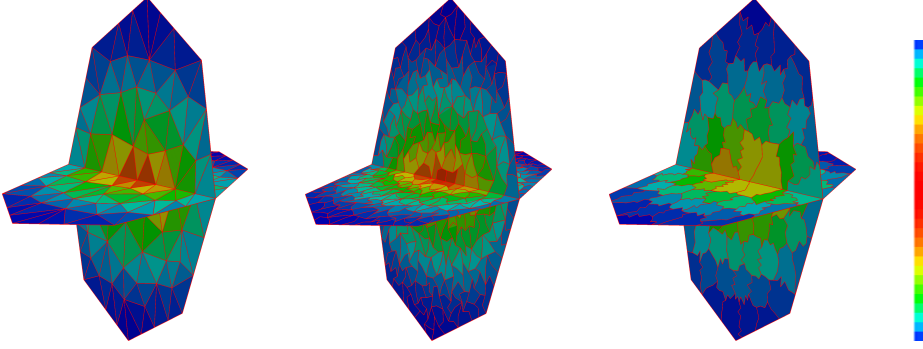


FIG. 15. Example of meshes and numerical solutions for the example in subsection 6.2.3. From the left: triangular mesh, coarse mesh with $c_{depth} = 2$, and pressure in γ from the $c_{depth} = 2$ case. The solution has range in $[0, 1]$ in the fractures and in $[0, 1.25]$ in the intersection, a “Blue to Red Rainbow” colour map is used.

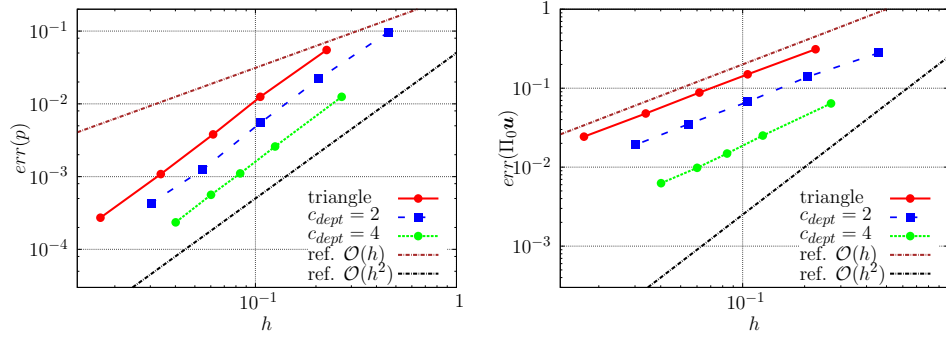


FIG. 16. In the figure the error decay for both p , in the left plot, and $\Pi_0 \mathbf{u}$ for the third example in subsection 6.2. We add the references $\mathcal{O}(h)$ and $\mathcal{O}(h^2)$ to easy the comparison.

6.3. Modeling of intersection flow. Having established the convergence properties of the virtual element method with and without flow in the intersection, we next focus on the modeling aspects of Problem 1 and Problem 2. To that end, we consider a network of four fractures, defined by

$$\begin{aligned} \Omega_1 &= \{(x, y, z) \in \mathbb{R}^3 : 0 \leq x \leq 1, y = 0, 0 \leq z \leq 1\} \\ \Omega_2 &= \text{rot}(\{(x, y, z) \in \mathbb{R}^3 : 1/5 \leq x - z \leq 6/5, -1/5 \leq x + z \leq 4/5, y = 0\}, \\ &\quad 2\pi/3, (1/2, 0, 0), (0, 0, 1)) \\ \Omega_3 &= \text{rot}(\{(x, y, z) \in \mathbb{R}^3 : \nu \leq x \leq 1/2 - \nu, y = 0, 1/2 + \nu \leq z \leq 1 + \nu, \}, \\ &\quad \pi/6, (1/2, 0, 1/2), (1, 0, -1)) \\ \Omega_4 &= \text{rot}(\{(x, y, z) \in \mathbb{R}^3 : 1/2 + \nu \leq x \leq 1 + \nu, y = 0, 1/2 + \nu \leq z \leq 1 + \nu, \}, \\ &\quad \pi/6, (1/2, 0, 1/2), (1, 0, -1)). \end{aligned}$$

Here we have introduced the short-form $\nu = 1/(5\sqrt{2})$ and $\text{rot}(\omega, \theta, v, w)$ denotes the rotation of domain ω with an angle θ around the line parametrized as $l(t) = v + wt$. The rotation angles are immaterial to the solution provided they are non-zero; the values chosen are motivated by clarity of visualization.

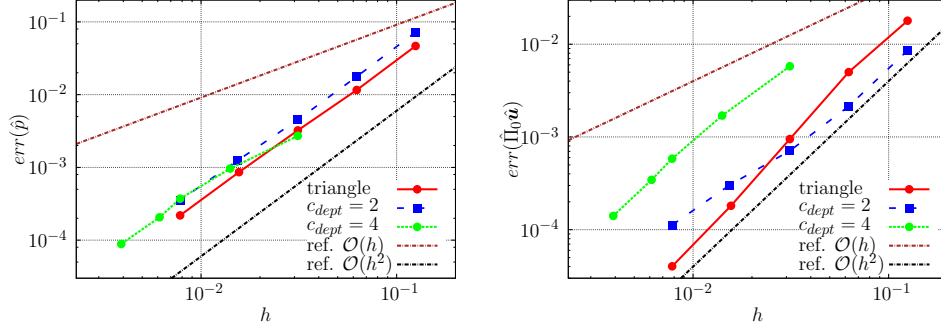


FIG. 17. In the figure the error decay for both \hat{p} , in the left plot, and $\hat{\Pi}_0 \hat{u}$ for the third example in subsection 6.2. We add the references $\mathcal{O}(h)$ and $\mathcal{O}(h^2)$ to easy the comparison.

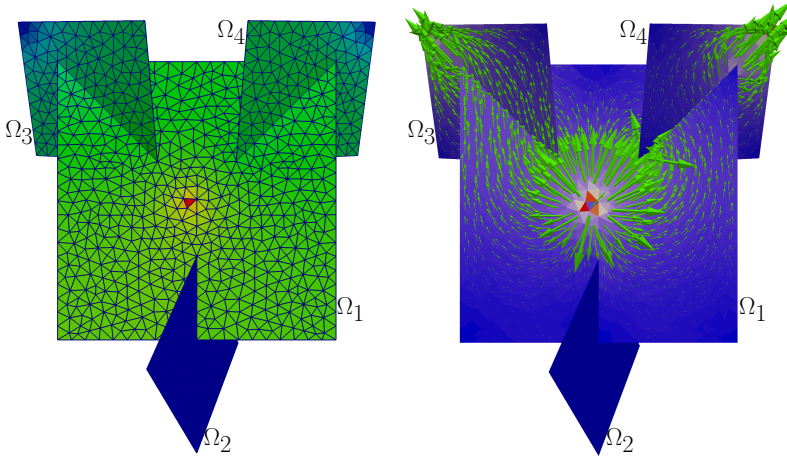


FIG. 18. Left: Pressure profile obtained for the family of four intersecting fractures. Right: Cell-wise velocity magnitudes, and also velocity vectors. Arrows close to the source and the outlets are not shown.

A source of unit strength is assigned in $(1/2, 0, 1/2)$, that is, in Ω_1 . For the other fractures, we assign homogeneous Dirichlet conditions on the faces in the corners furthest away from the injection points. On the remaining boundary edges we impose no-flux conditions. In terms of sources and boundary conditions, the problem is symmetric with respect to the fractures Ω_2 , Ω_3 and Ω_4 . We note that, due to the Neumann condition, this problem is outside the class considered in section 3.

In the intersection between Ω_1 and Ω_2 , the effective normal permeability $\tilde{\lambda}_m$ is set to 10^{-7} . The intersection between Ω_1 and Ω_3 has tangential effective permeability $\hat{\lambda}_k = 10^{-10}$, effectively employing Problem 1 here, while for the intersection of Ω_1 and Ω_4 , $\hat{\lambda}_k = 10^{10}$. All other permeabilities have unit value. Pressure and velocity profiles are shown in Figure 18. Due to the low $\tilde{\lambda}_m$, Ω_2 is effectively sealed off from the other fractures, with a pressure that is virtually equal to the outlet value in the entire fracture. The pressure difference between Ω_3 and Ω_4 is negligible. However, as seen from the velocity field, flow into Ω_4 is channelized into the intersection. For Ω_3 there is no flow in the intersection, but a wider sweep of the fracture plane itself compared to Ω_4 .

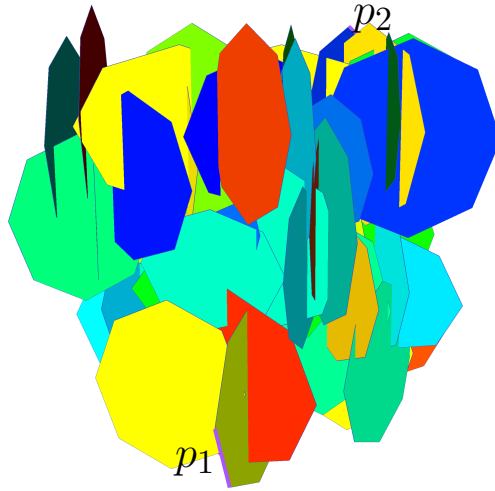


FIG. 19. Geometry used for the example in subsection 6.4. Each fracture is coloured by its identification number and the pressure boundary conditions are highlight using magenta segments.

6.4. Realistic DFN. In this final example, we illustrate the robustness of the approach for general fracture geometries. To that end, we consider a stochastically generated network of 60 fractures using the software described in [41]. The network is shown in Figure 19. The fracture permeability is set to unity, and for simplicity we only consider the model presented in Problem 1. Each fracture is discretized by 8 boundary edges, we impose no-flux boundary condition on all the edges of the fractures except for two of them. A pressure $p_1 = 1$ and $p_2 = 0$ is thus imposed. Again we note that the no-flow conditions are not covered by the analysis in section 3.

The stochastic generation of the fracture network leads to intersection configurations that may pose difficulties for meshing, in particular if the fracture planes are coupled during grid creation. Our approach of independent gridding of each fracture avoids the linkage of nodes in different fracture planes, but it still create small cells close to short constraints and almost parallel constraints. The coarsening algorithm, here applied with $c_{depth} = 2$ increases the cell size. The polygonal mesh has 24444 cells and 78574 edges, compared with 106809 cells for the triangular grid. The impact of the coarsening is illustrated in Figure 20.

Figure 21 shows the pressure solution and the projected velocity field, together a zoom-in in the vicinity of the outflow. As indicated by the figures, the numerical method captures high flow velocities in the in- and outflow fractures, as well as interaction between the fracture planes. It is worthwhile to consider how other conservative methods could have discretized the network in Figure 19. A key property of the virtual element method, and the closely related mimetic finite difference method, is the ability to handle hanging nodes and general polygon grids. A discretization by *e.g.* mixed finite elements would have required not only the triangular grid with about four times as many cells, but also techniques to eliminate hanging nodes at the intersections, which may further increase the cell number. Another possibility is to consider the class of finite volume methods which are, generally, more robust with respect to the shape of the cells. See for instance, [13].

7. Conclusions. In this paper we presented a novel approximation for a complex network of fractures using reduced models to describe fracture flows. The reduced

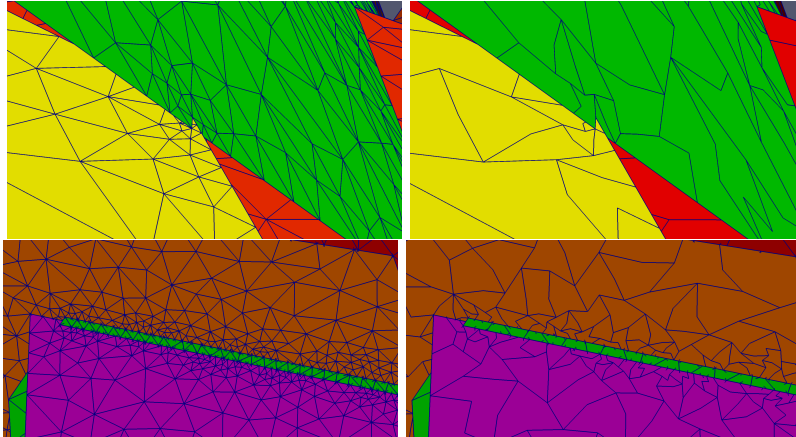


FIG. 20. Details of the mesh used in subsection 6.4. Left column: Original triangular grid. Right: Polygonal grid obtained after coarsening.

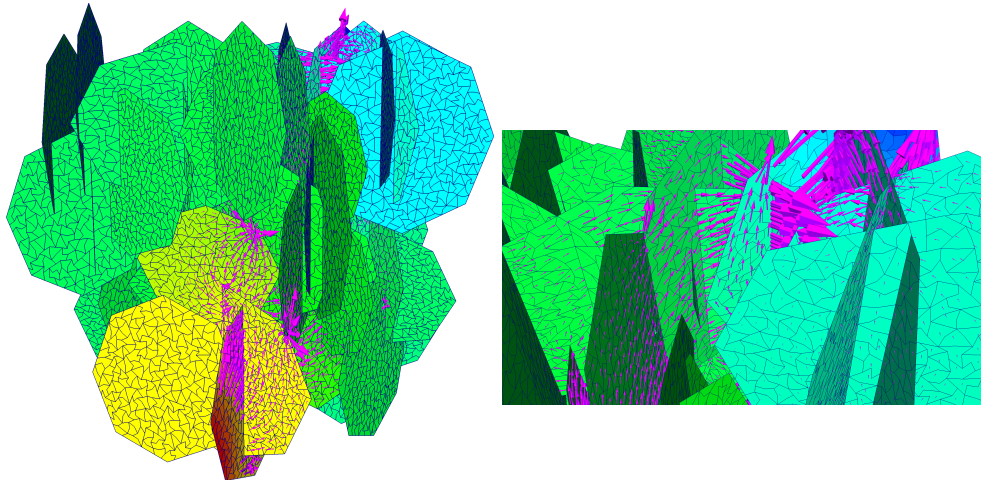


FIG. 21. Solution obtained with a realistic discrete fracture network. The figure depicts both pressure and velocity, the latter represented by magenta arrows. In the right the full system is represented while in the left a detail close to the outflow boundary is shown. The pressure has range in $[0, 1]$ and a “Blue to Red Rainbow” colour map is used. The velocity is restricted to ease the interpretation and the arrows are scaled with the velocity magnitude.

models are a reasonable approximation when the thickness of each fracture is some orders of magnitude smaller than its other characteristic sizes and smaller than the typical size of the surrounding rock matrix. In particular two models are presented to describe the flow at the intersection of fractures, with the possibility to allow a tangential flow along the intersection. The virtual element method’s ability to handle general polygons with hanging nodes allows us to relax constraints on the gridding of fracture intersections, and also apply grid coarsening. In the examples we saw the error decay of the solution, both pressure and Darcy velocity, behave as expected in all the cases. Finally we noticed that the solution behaves as expected and no evidence of serious contraindications is present, thus the algorithm presented seems a promising tool for the numerical approximation for this type of problems.

Acknowledgment. We acknowledge financial support for the ANIGMA project from the Research Council of Norway (project no. 244129/E20) through the EN-ERGIX program. The authors warmly thank the others components of the ANIGMA project team: Eivind Bastesen, Inga Berre, Simon John Buckley, Casey Nixon, David Peacock, Atle Rotevatn, Pål Næverlid Sævik, Luisa F. Zuluaga. The authors wish to thank also: Lourenço Beirão da Veiga, Wietse Boon, Franco Dassi, Luca Formaggia, Eren Uçar.

Appendix A. Details of coarsening algorithm.

Here we describe the coarsening algorithm in some detail. For further information, confer [39]. Define two parameters $\epsilon_{str} \in (0, 1)$ and $c_{depth} \in \mathbb{N}$. An element i , called C -element, in the original mesh will be connected, in the coarse grid, to some elements in the set N_i , called F -elements, those affect the error at i most. Since the algorithm is matrix base the previous request aim to find the F -elements j such that $|[A]_{ij}|$ is the largest in some sense. We say that a degree of freedom i is “strongly negatively coupled” (SNC) to j if

$$-[A]_{ij} \geq \epsilon_{str} \max_{[A]_{ik} < 0} |[A]_{ik}| \quad \text{and we have} \quad S_i := \{j \in N_i : i \text{ is SNC to } j\}.$$

Since the relation of being SNC is not symmetric we introduce $S_i^\top := \{j : i \in S_j\}$, which is the set of elements which are strongly coupled to i . Starting from a C -element i the algorithm connect all the F -elements j that are strongly coupled to i to create a coarse element. The process is repeated considering another C -element of the mesh. As highlight in [39], the selection of a new C -element i is based on the measure of importance λ_i in the set of undecided elements U , *i.e.* nor C or F -elements. We define

$$\lambda_i := \#(S_i^\top \cap U) + 2\#(S_i^\top \cap F) \quad \text{with} \quad i \in U,$$

where F is the set of F -elements. The next C -element will be the element with greater λ_i . The presented algorithm is repeated for c_{depth} -times where the initial mesh is the coarse mesh obtained at the previous step. The greater c_{depth} the bigger will be elements in the final coarse grid.

REMARK 5. *As point out in [39] a reasonable value for ϵ_{str} is 0.25. We note also that in the case of permeability with strong anisotropy the final mesh is able to better represent the underling physic of the problem. See subsection 6.1 for a discussion.*

REMARK 6. *To avoid pathological shapes of elements during the coarsening process at the tip of the intersection we impose a priori the triangles, which share the tip of the intersection and have an edge on the intersection, as C -elements.*

Appendix B. Tables.

In this section we present the detailed values for the examples in section 6. In Table 1 are reported the values for the test of subsection 6.2.1. In Table 2 are reported the values for the test of subsection 6.2.2.

REFERENCES

- [1] C. ALBOIN, J. JAFFRÉ, J. E. ROBERTS, X. WANG, AND C. SERRES, *Domain Decomposition for some Transmission Problems in Flow in Porous Media*, in Numerical treatment of multiphase flows in porous media (Beijing, 1999), vol. 552 of Lecture Notes in Phys., Springer, Berlin, 2000, pp. 22–34, doi:10.1007/3-540-45467-5_2.
- [2] L. AMIR, M. KERN, V. MARTIN, AND J. E. ROBERTS, *Décomposition de domaine et préconditionnement pour un modèle 3D en milieu poreux fracturé*, in Proceeding of JANO 8, 8th conference on Numerical Analysis and Optimization, Dec. 2005. 2005.

Coarse mesh family									
#	h	$err(p)$	$\mathcal{O}(p)$	$err(\Pi_0\mathbf{u})$	$\mathcal{O}(\Pi_0\mathbf{u})$	$\min p$	$\max p$	size	sparsity
1	3.162e-1	3.340e-2	-	2.713e-1	-	3.434e-3	1.228	152	1.158e-1
2	1.581e-1	9.774e-3	1.773	9.639e-2	1.493	4.958e-4	1.2642	584	3.321e-2
3	7.906e-2	2.537e-3	1.946	3.067e-2	1.652	7.474e-5	1.2947	2288	8.885e-3
4	3.953e-2	6.348e-4	1.998	9.360e-3	1.712	1.049e-5	1.3193	9056	2.292e-3
5	1.976e-2	1.577e-4	2.009	2.839e-3	1.721	1.393e-6	1.3308	36032	5.806e-4
6	9.882e-3	3.921e-5	2.008	8.742e-4	1.699	1.795e-7	1.3335	143744	1.467e-4
Cartesian mesh family									
#	h	$err(p)$	$\mathcal{O}(p)$	$err(\Pi_0\mathbf{u})$	$\mathcal{O}(\Pi_0\mathbf{u})$	$\min p$	$\max p$	size	sparsity
1	1.414e-1	4.099e-2	-	1.936e-1	-	-7.991e-4	1.283	320	1.793e-2
2	7.071e-2	1.061e-2	1.949	5.923e-2	1.709	-2.346e-5	1.3055	1240	4.646e-3
3	3.535e-2	2.682e-3	1.984	1.715e-2	1.788	5.599e-7	1.3211	4880	1.234e-3
4	1.768e-2	6.728e-4	1.995	4.807e-3	1.835	2.797e-7	1.3291	19360	3.162e-4
5	8.839e-3	1.684e-4	1.999	1.319e-3	1.866	4.767e-8	1.3329	77120	7.96e-5
6	4.419e-4	4.211e-5	1.999	3.567e-4	1.887	6.738e-9	1.335	307840	2.02e-5
Random mesh family									
#	h	$err(p)$	$\mathcal{O}(p)$	$err(\Pi_0\mathbf{u})$	$\mathcal{O}(\Pi_0\mathbf{u})$	$\min p$	$\max p$	size	sparsity
1	1.171e-1	3.4794e-2	-	2.434e-1	-	-8.777e-4	1.2988	320	2.168e-2
2	4.675e-2	9.8991e-3	1.367	1.032e-1	0.933	1.684e-6	1.3159	1240	5.749e-3
3	1.975e-2	2.5395e-3	1.581	4.993e-2	0.844	8.565e-6	1.328	4880	1481e-3
4	8.188e-3	6.5716e-4	1.535	2.481e-2	0.794	1.920e-6	1.3335	19360	3761e-4
5	4.04e-3	1.6608e-4	1.947	1.247e-2	0.974	2.948e-7	1.3353	77120	9.475e-5
6	1.843e-3	4.2e-5	1.752	6.218e-3	0.887	2.4239e-08	1.3362	307840	2.378e-5
Triangular mesh family									
#	h	$err(p)$	$\mathcal{O}(p)$	$err(\Pi_0\mathbf{u})$	$\mathcal{O}(\Pi_0\mathbf{u})$	$\min p$	$\max p$	size	sparsity
1	8.86e-2	2.928e-2	-	3.435e-1	-	-1.449e-3	1.3089	428	1.224e-2
2	4.221e-2	7.238e-3	1.885	1.572e-1	1.024	-1.971e-4	1.3157	1627	3.266e-3
3	2.029e-2	1.775e-3	1.919	7.426e-2	1.024	-1.849e-5	1.3296	6616	8.098e-4
4	1.014e-2	4.265e-4	2.055	3.597e-2	1.045	-1.793e-6	1.3319	26405	2.037e-4
5	4.594e-3	1.078e-4	1.738	1.807e-2	0.869	-2.125e-7	1.3348	105000	5.133e-5
6	2.204e-3	2.771e-5	1.849	9.167e-3	0.924	-5.644e-8	1.3358	408068	1.322e-05

TABLE 1

For each table we report the values for the discretization (h), errors ($err(p)$ and $err(\Pi_0\mathbf{u})$) and order of convergence ($\mathcal{O}(p)$ and $\mathcal{O}(\Pi_0\mathbf{u})$) for the example in subsection 6.2. The last columns are devoted to the minimum and maximum principle, number of rows (or columns) of the matrix and sparsity. For the name used in each table, consider the terminology reported in the aforementioned subsection.

- [3] P. F. ANTONIETTI, L. B. DA VEIGA, D. MORA, AND M. VERANI, *A stream virtual element formulation of the Stokes problem on polygonal meshes*, SIAM Journal on Numerical Analysis, 52 (2014), pp. 386–404, doi:10.1137/13091141X.
- [4] J. BEAR, C.-F. TSANG, AND G. DE MARSILY, *Flow and contaminant transport in fractured rock*, Academic Press, San Diego, 1993.
- [5] L. BEIRÃO DA VEIGA, F. BREZZI, L. D. MARINI, AND A. RUSSO, *H(div) and H(curl)-conforming VEM*, ArXiv e-prints, (2014), arXiv:1407.6822.
- [6] L. BEIRÃO DA VEIGA, F. BREZZI, L. D. MARINI, AND A. RUSSO, *The hitchhiker’s guide to the virtual element method*, Mathematical Models and Methods in Applied Sciences, 24 (2014), pp. 1541–1573, doi:10.1142/S021820251440003X.
- [7] L. BEIRÃO DA VEIGA, F. BREZZI, L. D. MARINI, AND A. RUSSO, *Mixed virtual element methods for general second order elliptic problems on polygonal meshes*, ESAIM: M2AN, 50 (2016), pp. 727–747, doi:10.1051/m2an/2015067.
- [8] L. BEIRÃO DA VEIGA, F. BREZZI, AND D. L. MARINI, *Virtual elements for linear elasticity problems*, SIAM Journal on Numerical Analysis, 51 (2013), pp. 794–812, doi:10.1137/120874746, http://dx.doi.org/10.1137/120874746, arXiv:http://dx.doi.org/10.1137/120874746.
- [9] M. F. BENEDETTO, S. BERRONE, A. BORIO, S. PIERACCINI, AND S. SCIALÒ, *A hybrid mortar virtual element method for discrete fracture network simulations*, Journal of Computational Physics, 306 (2016), pp. 148 – 166, doi:http://dx.doi.org/10.1016/j.jcp.2015.11.034.

Triangular mesh family										
#	h	$err(p)$	$\mathcal{O}(p)$	$err(\Pi_0\mathbf{u})$	$\mathcal{O}(\Pi_0\mathbf{u})$	# faces	min p	max p	size	sparsity
1	2.261e-1	3.87e-2	-	3.022e-1	-	3,3,3	5.949e-3	3.6581	646	7.96e-3
2	1.058e-1	8.160e-3	2.048	1.452e-1	0.964	3,3,3	5.063e-4	3.8417	3014	1.75e-3
3	7.461e-2	4.209e-3	1.898	1.082e-1	0.843	3,3,3	5.492e-4	3.8612	6070	8.76e-4
4	6.163e-2	2.818e-3	2.099	8.737e-2	1.120	3,3,3	3.625e-4	3.8900	8902	5.99e-4
5	3.382e-2	8.337e-4	2.029	4.881e-2	0.970	3,3,3	9.553e-5	3.9453	29626	1.81e-4
6	2.404e-2	4.235e-4	1.984	3.447e-2	1.019	3,3,3	3.394e-5	3.9620	58233	9.23e-5
Coarse mesh family with $c_{depth} = 2$										
#	h	$err(p)$	$\mathcal{O}(p)$	$err(\Pi_0\mathbf{u})$	$\mathcal{O}(\Pi_0\mathbf{u})$	# faces	min p	max p	size	sparsity
1	4.586e-1	9.771e-2	-	3.484e-1	-	5,6,9	5.135e-3	3.5731	268	3.659e-2
2	2.070e-1	2.080e-2	1.945	1.46e-1	1.094	5,6,9	3.256e-3	3.6826	1192	9.215e-3
3	1.474e-1	1.11e-2	1.85	1.016e-1	1.066	5,6,9	7.392e-4	3.8070	2366	4.725e-3
4	1.229e-1	7.212e-3	2.368	8.558e-2	0.943	5,6,9	1.016e-3	3.8260	3422	3.304e-3
5	6.705e-2	2.164e-3	1.987	4.469e-2	1.073	5,6,9	4.978e-4	3.8962	11238	1.029e-3
6	4.775e-2	1.093e-3	2.011	3.168e-2	1.013	5,6,9	1.828e-4	3.9359	21943	5.328e-4
Coarse mesh family with $c_{depth} = 4$										
#	h	$err(p)$	$\mathcal{O}(p)$	$err(\Pi_0\mathbf{u})$	$\mathcal{O}(\Pi_0\mathbf{u})$	# faces	min p	max p	size	sparsity
1	4.047e-1	2.075e-2	-	8.634e-2	-	17,20,25	3.824e-2	3.3361	758	3.960e-2
2	2.686e-1	9.821e-3	1.825	5.670e-2	1.026	13,19,24	9.755e-3	3.6202	1528	2.002e-2
3	1.973e-1	5.200e-3	2.06	3.255e-2	1.798	14,20,26	6.993e-3	3.6896	2792	1.168e-2
4	1.392e-1	2.525e-3	2.072	2.540e-2	0.711	13,20,26	2.891e-3	3.7927	5354	6.346e-3
5	9.758e-2	1.198e-3	2.099	1.569e-2	1.357	14,20,27	1.282e-3	3.8650	10537	3.283e-3
6	6.917e-2	6.154e-4	1.936	1.121e-2	0.976	13,20,26	6.152e-4	3.9082	20554	1.734e-3
Coarse mesh family with $c_{depth} = 5$										
#	h	$err(p)$	$\mathcal{O}(p)$	$err(\Pi_0\mathbf{u})$	$\mathcal{O}(\Pi_0\mathbf{u})$	# faces	min p	max p	size	sparsity
1	7.449e-1	4.609e-2	-	2.371e-1	-	29,38,48	9.882e-2	2.4769	520	9.531e-2
2	4.761e-1	2.827e-2	1.091	1.538e-1	0.967	28,36,44	6.912e-2	3.1075	890	5.795e-2
3	3.429e-1	1.313e-2	2.336	8.447e-2	1.825	18,35,49	2.227e-2	3.4482	1644	3.221e-2
4	2.515e-1	7.052e-3	2.005	5.368e-2	1.462	25,37,47	2.055e-2	3.5211	2942	2.003e-2
5	1.773e-1	3.138e-3	2.316	3.355e-2	1.345	21,37,49	9.645e-3	3.6361	5725	1.056e-2
6	1.27e-1	1.630e-3	1.962	2.577e-2	0.79	24,37,44	2.642e-3	3.8138	10908	5.841e-3

TABLE 2

For each table we report the values for the discretization (h), errors ($err(p)$ and $err(\Pi_0\mathbf{u})$) and order of convergence ($\mathcal{O}(p)$ and $\mathcal{O}(\Pi_0\mathbf{u})$) for the example in subsection 6.2.2. The last columns are devoted to the number of faces for each cell (minimum, average, and maximum, respectively), the minimum and maximum principle, number of rows of the matrix and sparsity. For the name used in each table, consider the terminology reported in the aforementioned subsection.

[10] M. F. BENEDETTO, S. BERRONE, S. PIERACCINI, AND S. SCIALÒ, *The virtual element method for discrete fracture network simulations*, Computer Methods in Applied Mechanics and Engineering, 280 (2014), pp. 135–156, doi:<http://dx.doi.org/10.1016/j.cma.2014.07.016>.

[11] S. BERRONE, S. PIERACCINI, AND S. SCIALÒ, *On simulations of discrete fracture network flows with an optimization-based extended finite element method*, SIAM Journal on Scientific Computing, 35 (2013), pp. 908–935, doi:[10.1137/120882883](https://doi.org/10.1137/120882883).

[12] W. M. BOON AND J. M. NORDBOTTEN, *Robust discretization of flow in fractured porous media*, ArXiv e-prints, (2016), arXiv:[1601.06977](https://arxiv.org/abs/1601.06977).

[13] K. BRENNER, J. HENNICKER, R. MASSON, AND P. SAMIER, *Gradient discretization of hybrid-dimensional Darcy flow in fractured porous media with discontinuous pressures at matrix-fracture interfaces*, IMA Journal of Numerical Analysis, (2016), doi:[10.1093/imanum/drw044](https://doi.org/10.1093/imanum/drw044).

[14] F. BREZZI, R. S. FALK, AND D. L. MARINI, *Basic principles of mixed virtual element methods*, ESAIM: M2AN, 48 (2014), pp. 1227–1240, doi:[10.1051/m2an/2013138](https://doi.org/10.1051/m2an/2013138).

[15] F. BREZZI AND M. FORTIN, *Mixed and Hybrid Finite Element Methods*, vol. 15 of Computational Mathematics, Springer Verlag, Berlin, 1991.

[16] C. D'ANGELO AND A. SCOTTI, *A mixed finite element method for Darcy flow in fractured porous media with non-matching grids*, Mathematical Modelling and Numerical Analysis, 46 (2012), pp. 465–489, doi:[10.1051/m2an/2011148](https://doi.org/10.1051/m2an/2011148).

[17] G. DZIUK, *Finite Elements for the Beltrami operator on arbitrary surfaces*, in Partial

Triangular mesh family										
#	h	$err(p)$	$\mathcal{O}(p)$	$err(\Pi_0 \mathbf{u})$	$\mathcal{O}(\Pi_0 \mathbf{u})$	# faces	min p	max p	size	sparsity
1	2.261e-1	5.494e-2	-	3.112e-1	-	3,3,3	6.051e-3	9.139e-1	655	7.871e-3
2	1.058e-1	1.249e-2	1.95	1.497e-1	0.963	3,3,3	5.141e-4	9.606e-1	3031	1.746e-3
3	6.163e-2	3.807e-3	2.2	8.795e-2	0.985	3,3,3	3.632e-4	9.723e-1	8935	5.974e-4
4	3.382e-2	1.082e-3	2.1	4.784e-2	1.01	3,3,3	9.558e-5	9.809e-1	29691	1.807e-4
5	1.695e-2	2.722e-4	2	2.434e-2	0.978	3,3,3	3.867e-5	9.913e-1	117311	4.588e-5
Coarse mesh family with $c_{depth} = 2$										
#	h	$err(p)$	$\mathcal{O}(p)$	$err(\Pi_0 \mathbf{u})$	$\mathcal{O}(\Pi_0 \mathbf{u})$	# faces	min p	max p	size	sparsity
1	4.586e-1	9.705e-2	-	2.802e-1	-	5,6,8	4.628e-3	8.183e-1	277	3.499e-2
2	2.070e-1	2.211e-2	1.86	1.393e-1	0.88	5,6,9	3.253e-3	9.152e-1	1209	9.036e-3
3	1.058e-1	5.478e-3	2.08	6.718e-2	1.09	5,6,9	3.466e-4	9.638e-1	4573	2.466e-3
4	5.461e-2	1.246e-3	2.24	3.519e-2	0.977	5,6,9	5.242e-4	9.777e-1	16761	6.928e-4
5	3.033e-2	4.337e-4	1.79	1.928e-2	1.02	5,6,10	5.833e-5	9.889e-1	54617	2.147e-4
Coarse mesh family with $c_{depth} = 4$										
#	h	$err(p)$	$\mathcal{O}(p)$	$err(\Pi_0 \mathbf{u})$	$\mathcal{O}(\Pi_0 \mathbf{u})$	# faces	min p	max p	size	sparsity
1	2.686e-1	1.249e-2	-	6.404e-2	-	13,19,24	9.662e-3	8.496e-1	1561	1.927e-2
2	1.253e-1	2.592e-3	2.06	2.509e-2	1.23	14,20,27	3.294e-3	9.399e-1	6649	5.112e-3
3	8.399e-2	1.107e-3	2.13	1.489e-2	1.31	14,20,30	7.368e-4	9.630e-1	14385	2.438e-3
4	6.012e-2	5.624e-4	2.02	9.809e-3	1.25	12,20,17	7.374e-4	9.797e-1	27537	1.294e-3
5	4.013e-2	2.352e-4	2.16	6.26e-3	1.11	13,20,27	1.825e-4	9.831e-1	60851	5.944e-4

TABLE 3

For each table we report the values for the discretization (h), errors ($err(p)$ and $err(\Pi_0 \mathbf{u})$) and order of convergence ($\mathcal{O}(p)$ and $\mathcal{O}(\Pi_0 \mathbf{u})$) for the example in [subsection 6.2.3](#). The last columns are devoted to the number of faces for each cell (minimum, average, and maximum, respectively), the minimum and maximum principle, number of rows of the matrix and sparsity. For the name used in each table, consider the terminology reported in the aforementioned subsection.

Triangular mesh family							
#	h	$err(\hat{p})$	$\mathcal{O}(\hat{p})$	$err(\tilde{\Pi}_0 \hat{\mathbf{u}})$	$\mathcal{O}(\tilde{\Pi}_0 \hat{\mathbf{u}})$	min \hat{p}	max \hat{p}
1	1.250e-1	4.665e-2	-	1.793e-2	-	3.423e-1	1.269
2	6.250e-2	1.158e-2	2.01	5.010e-3	1.84	1.647e-1	1.254
3	3.125e-2	3.229e-3	1.84	9.500e-4	2.4	8.042e-2	1.252
4	1.562e-2	8.601e-4	1.91	1.812e-4	2.39	3.966e-2	1.250
5	7.812e-3	2.187e-4	1.97	4.028e-5	2.17	1.968e-2	1.250
Coarse mesh family with $c_{depth} = 2$							
#	h	$err(\hat{p})$	$\mathcal{O}(\hat{p})$	$err(\tilde{\Pi}_0 \hat{\mathbf{u}})$	$\mathcal{O}(\tilde{\Pi}_0 \hat{\mathbf{u}})$	min \hat{p}	max \hat{p}
1	1.250e-1	7.198e-2	-	8.557e-3	-	3.524e-1	1.303
2	6.250e-2	1.769e-2	2.02	2.143e-3	2	1.658e-1	1.262
3	3.125e-2	4.511e-3	1.97	7.088e-4	1.6	8.061e-2	1.253
4	1.538e-2	1.246e-3	1.82	3.032e-4	1.2	3.967e-2	1.251
5	7.812e-3	3.541e-4	1.86	1.124e-4	1.47	1.968e-2	1.250
Coarse mesh family with $c_{depth} = 4$							
#	h	$err(\hat{p})$	$\mathcal{O}(\hat{p})$	$err(\tilde{\Pi}_0 \hat{\mathbf{u}})$	$\mathcal{O}(\tilde{\Pi}_0 \hat{\mathbf{u}})$	min \hat{p}	max \hat{p}
1	3.125e-2	2.717e-3	-	5.785e-3	-	8.066e-2	1.246
2	1.408e-2	9.627e-4	1.3	1.703e-3	1.53	3.965e-2	1.248
3	7.812e-3	3.718e-4	1.61	5.831e-4	1.82	1.968e-2	1.249
4	6.135e-3	2.059e-4	2.45	3.448e-4	2.17	1.968e-2	1.25
5	3.906e-3	8.863e-5	1.87	1.411e-4	1.98	9.803e-3	1.25

TABLE 4

For each table we report the values for the discretization (h), errors ($err(\hat{p})$ and $err(\tilde{\Pi}_0 \hat{\mathbf{u}})$) and order of convergence ($\mathcal{O}(\hat{p})$ and $\mathcal{O}(\tilde{\Pi}_0 \hat{\mathbf{u}})$) for the example in [subsection 6.2.3](#). The mesh size is referred to the intersection mesh. For the name used in each table, consider the terminology reported in the aforementioned subsection.

- Differential Equations and Calculus of Variations, S. Hildebrandt and R. Leis, eds., vol. 1357 of Lecture Notes in Mathematics, Springer Berlin Heidelberg, 1988, pp. 142–155, doi:10.1007/BFb0082865.
- [18] B. FAYBISHENKO, P. A. WITHERSPOON, AND S. M. BENSON, *Dynamics of fluids in fractured rock*, vol. 122 of Geophysical monographs, American geophysical union, 2000.
- [19] B. FLEMISCH, A. FUMAGALLI, AND A. SCOTTI, *A Review of the XFEM-Based Approximation of Flow in Fractured Porous Media*, vol. 12 of SEMA SIMAI Springer Series, Springer International Publishing, Cham, 2016, ch. Advances in Discretization Methods, pp. 47–76, doi:10.1007/978-3-319-41246-7_3.
- [20] L. FORMAGGIA, A. FUMAGALLI, A. SCOTTI, AND P. RUFFO, *A reduced model for Darcy’s problem in networks of fractures*, ESAIM: Mathematical Modelling and Numerical Analysis, 48 (2014), pp. 1089–1116, doi:10.1051/m2an/2013132.
- [21] N. FRIH, J. E. ROBERTS, AND A. SAADA, *Modeling fractures as interfaces: a model for Forchheimer fractures*, Computers and Geosciences, 12 (2008), pp. 91–104, doi:10.1007/s10596-007-9062-x.
- [22] A. FUMAGALLI AND A. SCOTTI, *An Efficient XFEM Approximation of Darcy Flows in Arbitrarily Fractured Porous Media*, Oil and Gas Sciences and Technologies - Revue d’IFP Energies Nouvelles, 69 (2014), pp. 555–564, doi:10.2516/ogst/2013192.
- [23] P. GRISVARD, *Singularities in Boundary Value Problems*, vol. 22 of Recherches en mathématiques appliquées, Springer-Verlag, 1992, <https://books.google.no/books?id=Kjqj-bAx4PYC>.
- [24] A. HANSBO AND P. HANSBO, *An unfitted finite element method, based on Nitsche’s method, for elliptic interface problems*, Comput. Methods Appl. Mech. Engrg., 191 (2002), pp. 5537–5552, doi:10.1016/S0045-7825(02)00524-8.
- [25] M.-H. HUI, B. T. MALLISON, AND K.-T. LIM, *An innovative workflow to model fractures in a giant carbonate reservoir*, in International Petroleum Technology Conference, 3–5 December, Kuala Lumpur, Malaysia, 2008, doi:10.2523/12572-MS.
- [26] J. D. HYMAN, C. W. GABLE, S. L. PAINTER, AND N. MAKEDONSKA, *Conforming Delaunay Triangulation of Stochastically Generated Three Dimensional Discrete Fracture Networks: A Feature Rejection Algorithm for Meshing Strategy*, SIAM Journal on Scientific Computing, 36 (2014), pp. A1871–A1894, doi:10.1137/130942541.
- [27] J. D. HYMAN, S. KARRA, N. MAKEDONSKA, C. W. GABLE, S. L. PAINTER, AND H. S. VISWANATHAN, *dfnWorks: A discrete fracture network framework for modeling subsurface flow and transport*, Computers & Geosciences, 84 (2015), pp. 10–19, doi:10.1016/j.cageo.2015.08.001.
- [28] M. KARIMI-FARD AND L. DURLOFSKY, *A general gridding, discretization, and coarsening methodology for modeling flow in porous formations with discrete geological features*, Advances in Water Resources, 96 (2016), pp. 354–372, doi:10.1016/j.advwatres.2016.07.019.
- [29] M. KARIMI-FARD, B. GONG, AND L. J. DURLOFSKY, *Generation of coarse-scale continuum flow models from detailed fracture characterizations*, Water Resources Research, 42 (2006), doi:10.1029/2006WR005015, <http://dx.doi.org/10.1029/2006WR005015>.
- [30] P. KNABNER AND J. E. ROBERTS, *Mathematical analysis of a discrete fracture model coupling Darcy flow in the matrix with Darcy-Forchheimer flow in the fracture*, ESAIM: Mathematical Modelling and Numerical Analysis, 48 (2014), pp. 1451–1472, doi:10.1051/m2an/2014003.
- [31] K.-A. LIE, S. KROGSTAD, I. S. LIGAARDEN, J. R. NATVIG, H. M. NILSEN, AND B. SKAFLESTAD, *Open-source MATLAB implementation of consistent discretisations on complex grids*, Computational Geosciences, 16 (2012), pp. 297–322, doi:10.1007/s10596-011-9244-4.
- [32] V. MARTIN, J. JAFFRÉ, AND J. E. ROBERTS, *Modeling Fractures and Barriers as Interfaces for Flow in Porous Media*, SIAM J. Sci. Comput., 26 (2005), pp. 1667–1691, doi:10.1137/S1064827503429363.
- [33] H. MUSTAPHA AND K. MUSTAPHA, *A New Approach to Simulating Flow in Discrete Fracture Networks with an Optimized Mesh*, SIAM Journal on Scientific Computing, 29 (2007), pp. 1439–1459, doi:10.1137/060653482.
- [34] D. C. PEACOCK, C. W. NIXON, A. ROTEVATN, D. J. SANDERSON, AND L. F. ZULUAGA, *Interacting faults*, Journal of Structural Geology, 97 (2017), pp. 1 – 22, doi:http://dx.doi.org/10.1016/j.jsg.2017.02.008.
- [35] S. PIERACCINI AND S. SCIALÒ, *Advances in Discretization Methods*, vol. 12 of SEMA-SIMAI Springer Series on Applied and Industrial Mathematics, Springer, 2016, ch. On a PDE-Constrained Optimization Approach for Flow Simulations in Fractured Media, pp. 27–45, doi:10.1007/978-3-319-41246-7.
- [36] A. ROTEVATN, S. J. BUCKLEY, J. A. HOWELL, AND H. FOSSEN, *Overlapping faults and their*

- effect on fluid flow in different reservoir types: A LIDAR-based outcrop modeling and flow simulation study*, AAPG Bulletin, (2009), doi:10.1306/09300807092.
- [37] N. SCHWENCK, B. FLEMISCH, R. HELMIG, AND B. WOHLMUTH, *Dimensionally reduced flow models in fractured porous media: crossings and boundaries*, Computational Geosciences, 19 (2015), pp. 1219–1230, doi:10.1007/s10596-015-9536-1.
- [38] J. R. SHEWCHUK, *Triangle: Engineering a 2D Quality Mesh Generator and Delaunay Triangulator*, in Applied Computational Geometry: Towards Geometric Engineering, M. C. Lin and D. Manocha, eds., vol. 1148 of Lecture Notes in Computer Science, Springer-Verlag, May 1996, pp. 203–222. From the First ACM Workshop on Applied Computational Geometry.
- [39] U. TROTTENBERG, C. W. OOSTERLEE, AND A. SCHÜLLER, *Multigrid*, Elsevier Academic Press, 2001.
- [40] C. XIANG, X. PANG, W. YANG, J. WANG, Q. LI, L. LIU, AND Y. LI, *Hydrocarbon migration and accumulation along the fault intersection zone—a case study on the reef-flat systems of the no.1 slope break zone in the tazhong area, tarim basin*, Petroleum Science, 7 (2010), pp. 211–225, doi:10.1007/s12182-010-0021-0.
- [41] C. XU AND P. DOWD, *A new computer code for discrete fracture network modelling*, Computers & Geosciences, 36 (2010), pp. 292 – 301, doi:https://doi.org/10.1016/j.cageo.2009.05.012.